

RESEARCH ARTICLE

10.1002/2013JD020673

Key Points:

- Convective overshoot properties differ between monsoon regimes over Darwin
- C-POL radar statistics contain biases in the TTL
- C-POL radar underestimates storm overshooting area in the TTL

Correspondence to:

M. E. E. Hassim,
mehassim@unimelb.edu.au

Citation:

Hassim, M. E. E., T. P. Lane, and P. T. May (2014), Ground-based observations of overshooting convection during the Tropical Warm Pool-International Cloud Experiment, *J. Geophys. Res. Atmos.*, 119, 880–905, doi:10.1002/2013JD020673.

Received 8 AUG 2013

Accepted 15 DEC 2013

Accepted article online 18 DEC 2013

Published online 29 JAN 2014

Ground-based observations of overshooting convection during the Tropical Warm Pool-International Cloud Experiment

M. E. E. Hassim^{1,2}, T. P. Lane^{1,2}, and P. T. May³
¹School of Earth Sciences, University of Melbourne, Melbourne, Victoria, Australia, ²ARC Centre of Excellence for Climate System Science, University of New South Wales, Sydney, New South Wales, Australia, ³Centre for Australian Weather and Climate Research, Bureau of Meteorology, Docklands, Victoria, Australia

Abstract This study uses gridded radar data to investigate the properties of deep convective storms that penetrate the tropical tropopause layer (TTL) and overshoot the cold-point tropopause during the Tropical Warm Pool-International Cloud Experiment (TWP-ICE). Overshooting convection during the observed break period is relatively more intense and exhibits lesser diurnal variability than severe monsoonal storms in terms of mean overshooting area in the TTL (as covered by >20 dBZ echoes). However, ground-based radar has geometrical constraints and sampling gaps at high altitude that lead to biases in the final radar product. Using synthetic observations derived from model-based data, ground-based radar is shown to underestimate the mean overshooting area in the TTL across both TWP-ICE regimes. Differences range from ~180 km² (~100 km²) to ~14 km² (~8 km²) between 14 and 18 km for the active (break) period. This implies that the radar is underestimating the transport of water and ice mass into the TTL by convective overshoots during TWP-ICE. The synthetic data is also used to correct profiles of the mean observed overshooting area. These are shown to differ only marginally between the two sampled regimes once the influence of a large mesoscale convective system, considered as a departure from normal monsoon behavior, was removed from the statistics. The results of our study provide a useful cross-validation comparison for satellite-based detections of overshooting top areas over Darwin, Australia.

1. Introduction

Overshooting deep convection in the tropics is known to influence the humidity of the tropical tropopause layer (TTL) on local scales [Jensen *et al.*, 2007; Hassim and Lane, 2010]. The TTL, herein defined as the layer between 14 and 18.5 km following Fueglistaler *et al.* [2009], is considered a zone that gradually separates the convectively driven troposphere from the radiatively driven stratosphere. Intense thunderstorms can directly inject water mass and other trace species into the TTL and potentially affect the moisture and chemical budgets when they overshoot into the tropical lower stratosphere. In recent years, the contribution of overshooting convection to tropical lower stratospheric humidity has been the subject of considerable attention [Toon *et al.*, 2010]. Previous numerical studies [e.g., Chaboureaud *et al.*, 2007; Chemel *et al.*, 2009; Liu *et al.*, 2010a] conclude that tropical overshoots can hydrate the lower stratosphere directly, supporting recent observational evidence [e.g., de Reus *et al.*, 2009; Corti *et al.*, 2008; Nielsen *et al.*, 2007]. Recent calculations from modeled events suggest that the moistening potential is related to the severity and properties of the overshoot [Grosvenor *et al.*, 2007; Liu *et al.*, 2010a].

In the Maritime Continent, some overshooting storms have been detected to reach as high as 19–20 km in altitude by ground-based radar [e.g., Simpson *et al.*, 1993; May and Keenan, 2005; May and Ballinger, 2007]. Accordingly, statistics such as the frequency, area, depth, and duration of convective overshoots are most useful. For example, the mean area of overshooting can be utilized in upscaling estimates to calculate the global convective input of water mass into the tropical stratosphere, relative to the large-scale upwelling flux and other known transport pathways.

The Tropical Warm Pool-International Cloud Experiment (TWP-ICE) was conducted in and around Darwin, Australia, from 19 January to 14 February 2006 to coincide with the height of the monsoon season [May *et al.*, 2008]. One major outcome of TWP-ICE was the provision of a comprehensive observational data set that included the sampling of four weather regimes: a convectively active monsoon (20–25 January),

a relatively suppressed monsoon (26 January to 2 February), three clear days (3–5 February), and finally a monsoon break period (6–13 February). TWP-ICE followed the joint Stratospheric-Climatic Links with Emphasis on the Upper Troposphere and Lower Stratosphere/Aerosol and Chemical Transport in Tropical Convection campaign, which was also conducted in the region surrounding Darwin from November to December 2005 [Vaughan *et al.*, 2008].

A primary source of observations during those field experiments was the C-band polarimetric radar (C-POL) situated at Gunn Point (12.25°E, 131.04°S), about 30 km northeast of Darwin [Keenan *et al.*, 1998]. With a temporal scanning resolution of 10 min and a maximum tilt elevation of 42°, C-POL has the potential to characterize the variability as well as the properties of overshooting convection. Overshoot statistics from C-POL observations can therefore help constrain the mean input of water into the TTL by intense thunderstorms in different convective regimes experienced during TWP-ICE.

Recently, Frederick and Schumacher [2008] used gridded C-POL observations to examine the anvil characteristics of convective clouds during the convectively active monsoon, the suppressed monsoon, and the break period regimes. Caine *et al.* [2013], May and Ballinger [2007], and Vallgren [2006] also used gridded C-POL data along with a cell-tracking algorithm to generate statistics of convective storms in different regimes, but they did not specifically focus on storm overshoot properties in the TTL. We seek to complement previous analyses by focusing on the subset of very deep convection that penetrated the TTL during the active and break phases of the 2006 Australian monsoon season. As will be shown, overshooting convection was constantly observed by the C-POL radar during the two convective regimes.

In this study, the gridded C-POL data set is utilized to examine the efficacy of ground-based radar in characterizing the nature of overshooting convection during both TWP-ICE regimes. According to Drosowsky [1996], the active monsoon phase in Darwin is largely characterized by westerly flow exceeding 10 m s^{-1} between the surface and 700 hPa, with onset being the date when the first sustained westerly wind burst occurred. In 2006, the active monsoon began on 10 January [May *et al.*, 2012]. However, a simpler definition of westerlies exceeding 10 m s^{-1} at 700 hPa was used during TWP-ICE, based on a 4 day smoothed wind time series [May *et al.*, 2008]. In contrast, break period conditions exhibited easterly flow throughout much of the troposphere. Since the nature of convection is known to be different in each phase [Keenan and Carbone, 1992; May and Rajopadhyaya, 1999; May and Ballinger, 2007], our objective here is to understand whether the bulk properties of overshooting convection vary considerably between the two large-scale regimes. A particular focus will be on the mean overshooting area as this will be most useful in upscaling estimates of overshooting mass flux.

Despite the potential to provide useful metrics, statistics obtained from ground-based radar are affected by limitations of the observing platform and the scanning strategy. Apart from sampling gaps at high altitude, radar measurements are also affected by the beam broadening at large distances. The spread of the beam with range is limited to the angular *beam width* of the radar (a fixed geometrical property of the system). This broadening effect may lead to partial beam filling at large distances, which reduces the mean reflectivity measured over the corresponding sample volume. This observational bias represents an inherent caveat that ultimately affects ground-based radar statistics, particularly at high levels. Such sampling biases are yet to be fully quantified for the TTL region.

Hence, this study also attempts to estimate and correct for biases found in gridded C-POL observations. Bias correction for the mean overshooting area is performed with guidance from synthetic sampling of model-derived reflectivity fields. These fields are calculated from cloud-system resolving Weather Research and Forecasting (WRF) model simulations of the two TWP-ICE regimes, which are then subjected to a radar-sampling emulation algorithm. This algorithm mimics the three-dimensional (3-D) geometry of the C-POL scanning strategy during TWP-ICE and accounts for the beam broadening with range.

The remainder of the paper is organized as follows. Section 2 presents a brief overview of the meteorology experienced during TWP-ICE. C-POL observations of overshooting events and statistics are shown in section 3. High-resolution WRF simulations for the active monsoon and break periods are then described in section 4, in which synthetic measurements of modeled reflectivity fields are used to highlight the observational biases. Section 5 proposes a bias correction method and presents altitude-dependent corrections to the mean overshooting area statistic derived from the gridded C-POL data for TWP-ICE. Finally, conclusions are summarized in section 6.

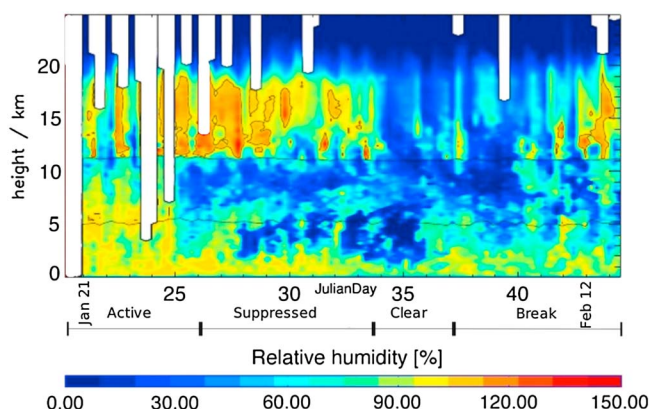


Figure 1. Time-height trace of relative humidity with respect to water (below 11 km) and ice (RHI; above 11 km) from radiosondes released every 3 h over Darwin during TWP-ICE (regimes labeled). Thin lines denote the freezing level (0°C , ~ 5 km) and the level of homogeneous nucleation (-40°C , ~ 11 km). Outlined colored contours denote where $\text{RHI} \geq 100\%$. White bars denote times of no data. The data have been dry-bias corrected according to the procedure outlined by Hume [2007].

2. Meteorology During TWP-ICE

A wide range of convective activity was sampled by C-POL during the three TWP-ICE convective regimes. During the active monsoon phase, convection was fairly widespread with varying degrees of organization. This period coincided with an active Madden-Julian Oscillation phase over northern Australia, which resulted in an area mean rainfall of $\sim 17 \text{ mm d}^{-1}$ and relatively thick cirrus within the domain [May *et al.*, 2008]. It was also characterized by high relative humidity throughout the depth of the troposphere and exhibited a TTL that was more often ice supersaturated compared to the break period (Figure 1). The high humidity and relatively large mean vertical motion in the active phase were consistent with the highest cloud frequencies being detected up to 16 km during this period [Wapler *et al.*, 2010].

Unusually suppressed monsoon conditions were experienced between 26 January and 2 February in which convective tops were limited to below 10 km due to the advection of drier midlevel air from the continent's interior by an inland tropical low-dubbed "Landphoon John" [May *et al.*, 2008]. Storms during this phase also exhibited little stratiform regions. Three clear quiescent days followed the suppressed monsoon before break period conditions developed from 6 February onward. During this phase, an inland heat trough dominated the region across northern Australia. Afternoon and early evening storms observed were deep, electrically active, and highly localized. These storms predominantly occurred over land and often initiated along the trough and sea-breeze boundaries before developing into convective squall lines overnight, driven by the easterly flow across the domain [Wapler *et al.*, 2010]. The area-averaged precipitation rate was about 8 mm d^{-1} due to break period convection being more transient and spatially localized [May *et al.*, 2008].

3. C-POL Reflectivity

The C-POL radar operates at a wavelength of 5.5 cm and completes a 3-D scan of the atmosphere once every 10 min through a sequence of conical sweeps at increasing elevations. Data are collected every 300 m along the 1° beam. In practice, C-POL has a horizontal viewing distance of 150 km radially. At this range, the minimum detectable signal is approximately 0 dBZ; thus, the radar is able to see a considerable amount of nonprecipitating cloud [May and Keenan, 2005]. Further details about the C-POL system characteristics are found in Keenan *et al.* [1998] and May and Keenan [2005].

For our analysis, we use gridded C-POL data that have been interpolated using the Sorted Position Radar Interpolation (SPRINT) software. The data consist of 40 vertical levels from 0.5 to 20 km. Each level is separated by a vertical spacing of 500 m and has 121×121 horizontal grid points distanced 2.5 km apart. The temporal resolution of the data is 10 min. Because clutter was found to be pervasive at the upper levels [Varble *et al.*, 2011], we restrict our analysis to values of 5 dBZ and greater.

The C-POL scanning strategy during TWP-ICE contained 17 elevation tilts from 0.5° to 42° (Figure 2). Notably, 11 tilts sampled the TTL and lower stratosphere (15–20 km). C-POL was therefore able to observe convective

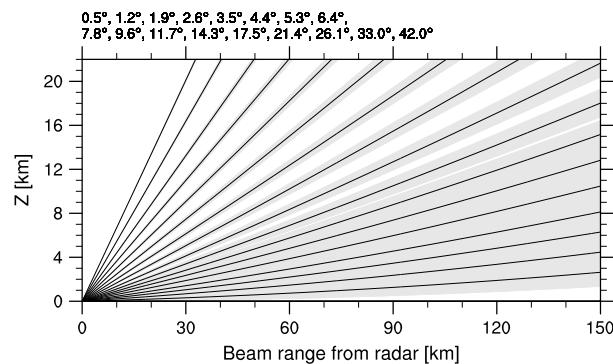


Figure 2. Beam coverage pattern for the C-POL radar during the TWP-ICE campaign. Black lines represent central beam axes while shaded grey areas represent the vertical beam spread with range for a beam width of 1°. Individual tilt elevation angles are shown at the top of the plot.

storms that reach the TTL. However, sampling the upper level portions of these high-reaching storms (e.g., between 15 and 18 km) is challenging due to large vertical separations between the higher tilts especially when storms are close to the radar. These sampling gaps cause upper level ring-like artifacts to appear when volumetric observations are interpolated onto a Cartesian grid. They are present where limits of echoes occur in orthogonal planes, such as along storm tops or when there is poor resolution in the observations [Mohr and Vaughan, 1979].

These sampling gaps affect the height assignment and lateral extent of detected echoes, resulting in inherent observational biases that are mainly due to the geometrical sampling constraints of the radar (see section 4.2). However, a more sophisticated interpolation algorithm like the Kriging method removes these upper level artifacts when volumetric C-POL data are gridded [Seed and Pegram, 2001]. This algorithm was used by May and Ballinger [2007] but is not yet applied routinely.

3.1. Observations

Figures 3 and 4 show horizontal cross sections of gridded C-POL reflectivity data at 14 km. These are shown for selected days during the active and break periods sampled during TWP-ICE, respectively. Both sets of radar imagery depict deep convection with intense cores penetrating the bottom of the TTL. Such convective cores are identified by echo values >20 dBZ and appear as distinct clusters of contiguous pixels embedded within the larger anvil stratiform areas. Henceforth, the 20 dBZ threshold is adopted as the cut-off value for identifying the area of overshooting in the TTL as they indicate the presence of precipitation-sized ice particles being lofted high up in altitude and are therefore evidence of strong convective updrafts. Furthermore, these clusters were found to be much less affected by ringed artifacts that may contaminate the upper level stratiform regions in the final radar data product. The choice of 20 dBZ as a cut-off value is also the same threshold used by Liu and Zipser [2005] to identify overshooting precipitation features in their study.

In the active monsoon examples, the total area covered by pixels >20 dBZ increases from 22 January onward. This represents the state of the overall environment, which became increasingly conducive to stronger and more organized deep convection. On 23 January, a large mesoscale convective system (MCS) propagated across the experiment domain in a westward direction [May et al., 2008]. The most organized and vigorous overshooting activity during TWP-ICE was observed during this time (Figures 3e and 3f). In contrast, echoes between 30 and 45 dBZ are consistently seen within the updraft cores of break period convection, indicating that larger ice particles are being lofted to this level by very strong updrafts (Figure 4). This is consistent with the gross characteristics of coastal, continental, and island-based (Hector) thunderstorms during the break period; they are generally more intense and spatially localized compared to storms during the active monsoon phase [Vallgren, 2006; May and Ballinger, 2007].

Daily features of the strongest convective events are contrasted in Figure 5. This figure plots the maximum reflectivity (Z_{\max}) observed at each vertical level between 14 and 20 km for both the active monsoon (Figures 5a and 5b) and the break period (Figures 5c and 5d). Note that Figure 5a shows Z_{\max} over a 5 day pre-TWP-ICE period starting 5 days after monsoon onset, while Z_{\max} observed during the active monsoon phase of TWP-ICE is shown in Figure 5b. Both regimes exhibit deep convection penetrating high into the

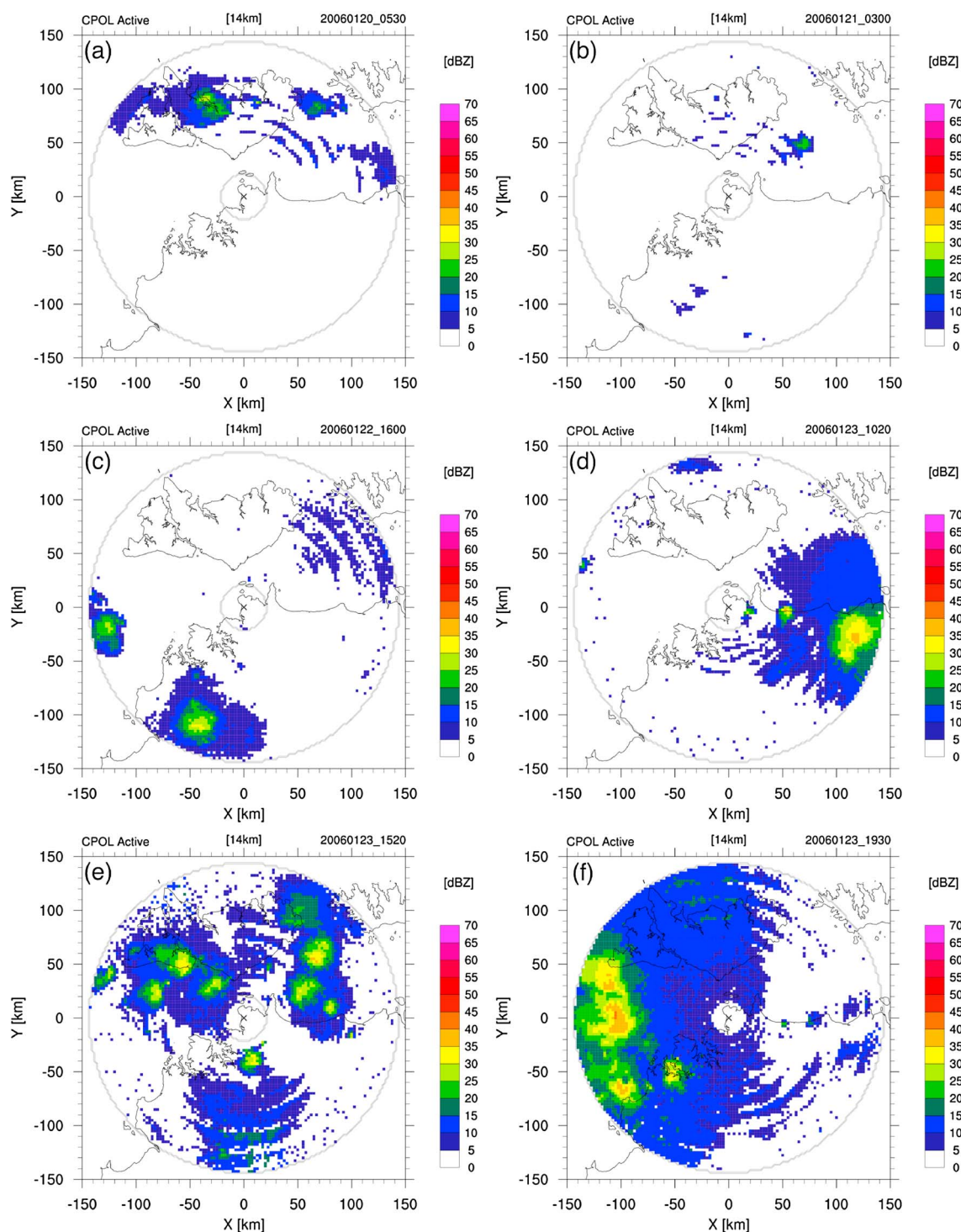


Figure 3. Examples of deep convection penetrating the TTL base at 14 km for selected days of the active monsoon phase during TWP-ICE. C-POL's position is marked by the "cross" and the radar's outer radial extent is denoted by the grey circle. Note that times shown are in Coordinated Universal Time (UTC; local Darwin time is UTC + 0930 h). The horizontal resolution of the data is 2.5 km.

TTL on a daily basis, with 20 dBZ echoes consistently reaching and occasionally overshooting the mean cold-point tropopause (CPT; ~ 17 km). Such behavior in the pre-TWP-ICE period (Figure 5a) is consistent with that found by May and Ballinger [2007], who noted that monsoon convective systems can and do reach the tropopause. However, most storms during the active phase were less intense than those in the break period. Indeed, Figure 5d shows that 30 dBZ echoes above the CPT are observed more often on a daily basis

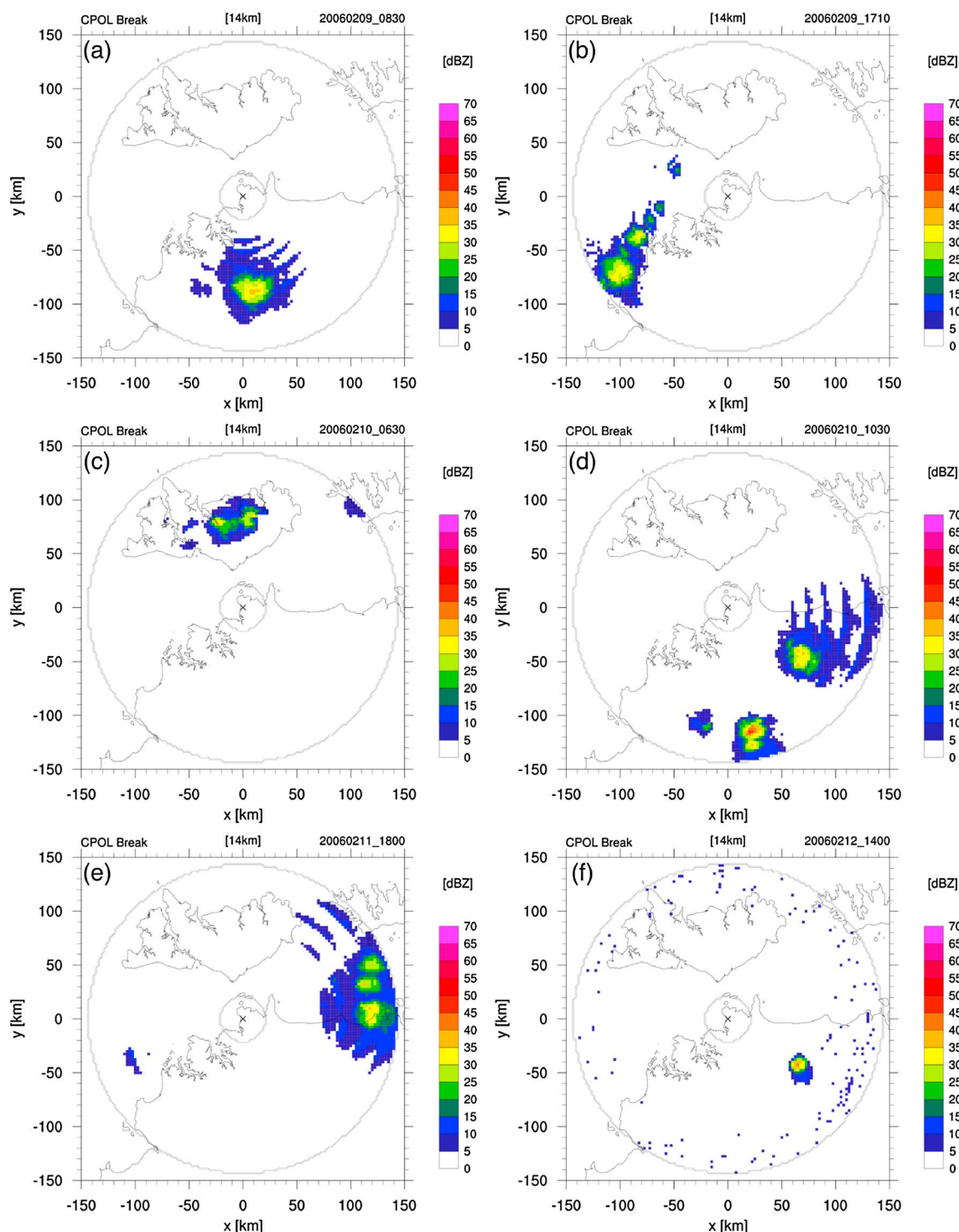


Figure 4. As in Figure 3 but for the selected days in the break period. Note the afternoon Hector thunderstorm over the Tiwi Islands on 10 February at 0630 UTC.

between 9 and 13 February than at any other time during the active monsoon period, except on 23 January (Figure 5b).

Figures 5e and 5f provide further statistical evidence of this regime difference by showing the frequency distribution of reflectivity values between 20 and 40 dBZ binned into 1 dBZ intervals at both 14 km and 17 km, respectively. At both these heights, occurrence statistics for the active monsoon are significantly dominated by the MCS event, such that they exceed those for the break period across all bins except for reflectivities

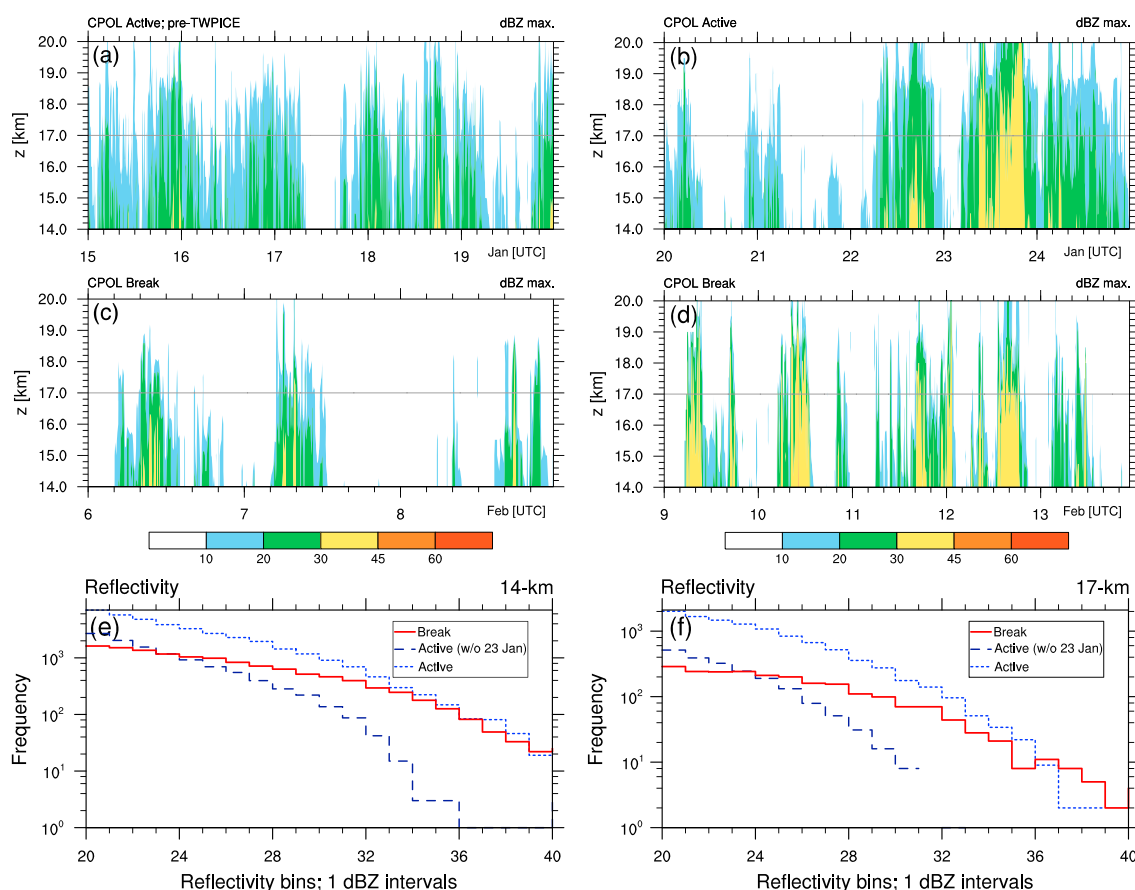


Figure 5. Maximum reflectivity (Z_{\max}) observed at each level between 14 and 20 km during the (a and b) active monsoon and (c and d) break period. The horizontal line denotes the approximate height of the mean cold-point tropopause (CPT) during TWP-ICE. The CPT is determined from the average height of the minima in temperature profiles obtained from bias-corrected 3-hourly Darwin radiosonde data. (e and f) Frequency of reflectivity values between 20 and 40 dBZ in 1 dBZ intervals at 14 km and 17 km height levels, respectively. Data shown in logarithmic scale.

>36 dBZ (Figure 5f). When frequencies are recomputed without 23 January, the new distribution clearly shows that deep monsoonal convection is less intense than break period convection, confirming the climatological characteristics of both regimes. Therefore, the MCS day can be regarded as a departure from normal monsoon behavior. Due to the short record analyzed in our study, statistics for the TWP-ICE active monsoon phase are heavily influenced by the severity and longevity of the overshooting associated with the MCS event (see section 3.2). The short observational record during TWP-ICE also prevents us from making any conclusive statements about the diurnal variation of deep convection reaching the TTL, as the unusual timings of several strong individual events skew the statistics from those expected from known climatology [e.g., Protat et al., 2010; May et al., 2012].

3.2. Statistics of Areal Coverage

The previous section highlighted differences in intensity between overshooting convection in the two regimes. Here we present statistics that relate to overshooting areal coverage as this has implications for estimates of convective mass flux into the tropical lower stratosphere.

We begin by summarizing the areal distribution of storm reflectivity values with height using contoured coverage altitude diagrams (CCAD) to further understand the relative differences between overshooting convection in both regimes. The CCAD is similar to the contoured frequency altitude diagrams used by Yuter and Houze [1995] except that reflectivity bin counts are divided by the total radar-observable area at each height level following Caine et al. [2009]. First, reflectivity values ranging from 5 to 75 dBZ are tallied in 5 dBZ wide bins (5–10, 10–15 dBZ, etc.). The fractional radar area covered by each bin is then found by dividing the aggregate number of counts by the total number of radar-observable grid points at each height level and expressed as a percentage. This gives us the areal coverage of each reflectivity bin with respect to all radar

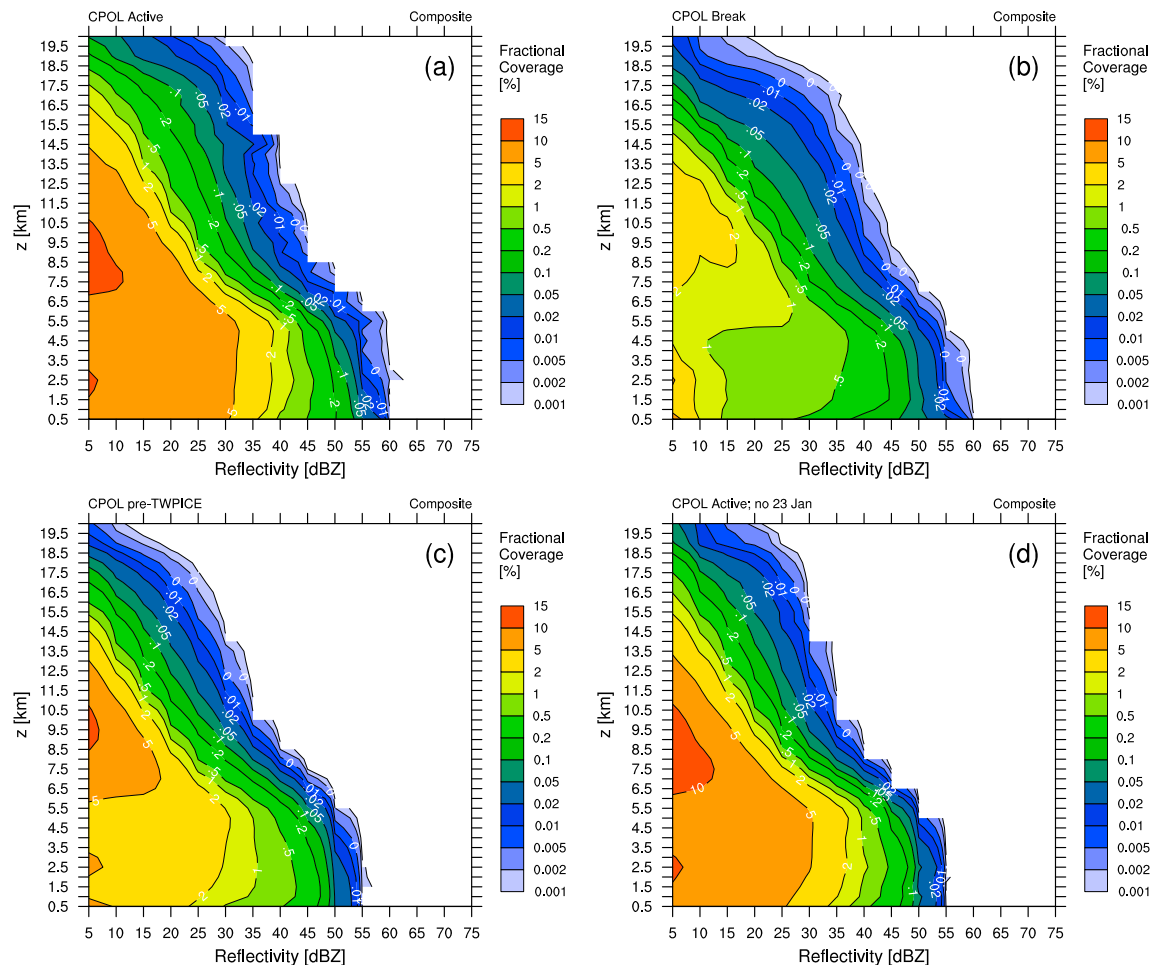


Figure 6. Composite CCADs for the TWP-ICE (a) active and (b) break periods. Also shown are the composite CCADs for the (c) pre-TWP-ICE active phase and (d) TWP-ICE active phase without the MCS day (23 January 2006).

pixels at that level. The same procedure is also applied to find the fractional coverage of reflectivities beyond a chosen threshold (e.g., >20 dBZ), which is useful for the analysis of overshooting area in the TTL.

Figures 6a and 6b display the composite CCADs for both the TWP-ICE active and break periods, respectively. The composite CCAD for the pre-TWP-ICE period of 15–19 January is also shown in Figure 6c, along with the composite CCAD for the TWP-ICE active period calculated without the MCS day of 23 January (Figure 6d). Each composite is the average of all daily mean CCADs in each corresponding period (not shown). The composite CCAD for the TWP-ICE active period (Figure 6a) indicates that the radar domain was covered more frequently by echoes that are representative of deep stratiform regions over much of the troposphere (e.g., 5% contour line for 20–30 dBZ between 0.5 and 8.5 km). The highest relative fractional areas are observed in the 5–10 dBZ bin between 7 and 10.5 km. These features are consistent with the large-scale ascent typical of the wet monsoon regime and the average anvil thicknesses and areal coverage identified by *Frederick and Schumacher* [2008]. Conversely, the highest fractional coverages in the break period occur between 7 and 13.5 km for reflectivities between 5 and 15 dBZ (Figure 6b). Both CCADs indicate that overshooting convection extended throughout the TTL, although slightly greater fractional areas are measured for the TWP-ICE active period than in the monsoon break (e.g., the maximum height of the 1% and 2% contours are 2.5 km and 3 km higher, respectively; c.f. Figures 6a and 6b). This is most likely due to the enhanced overshooting activity from the later half of 22 January onward and during the MCS day of 23 January (c.f. Figure 5b). The pre-TWP-ICE CCAD bears close resemblance to that of the TWP-ICE active period, except that tropospheric stratiform regions indicated by 20–30 dBZ echoes cover only about 2% of the radar domain up to 8.5 km (Figure 6c). Note, however, that fractional coverages of 20 and 30 dBZ echoes are lower at both 10 and 15 km when the atypical influence of the MCS day was removed (Figure 6d). This suggests that normal

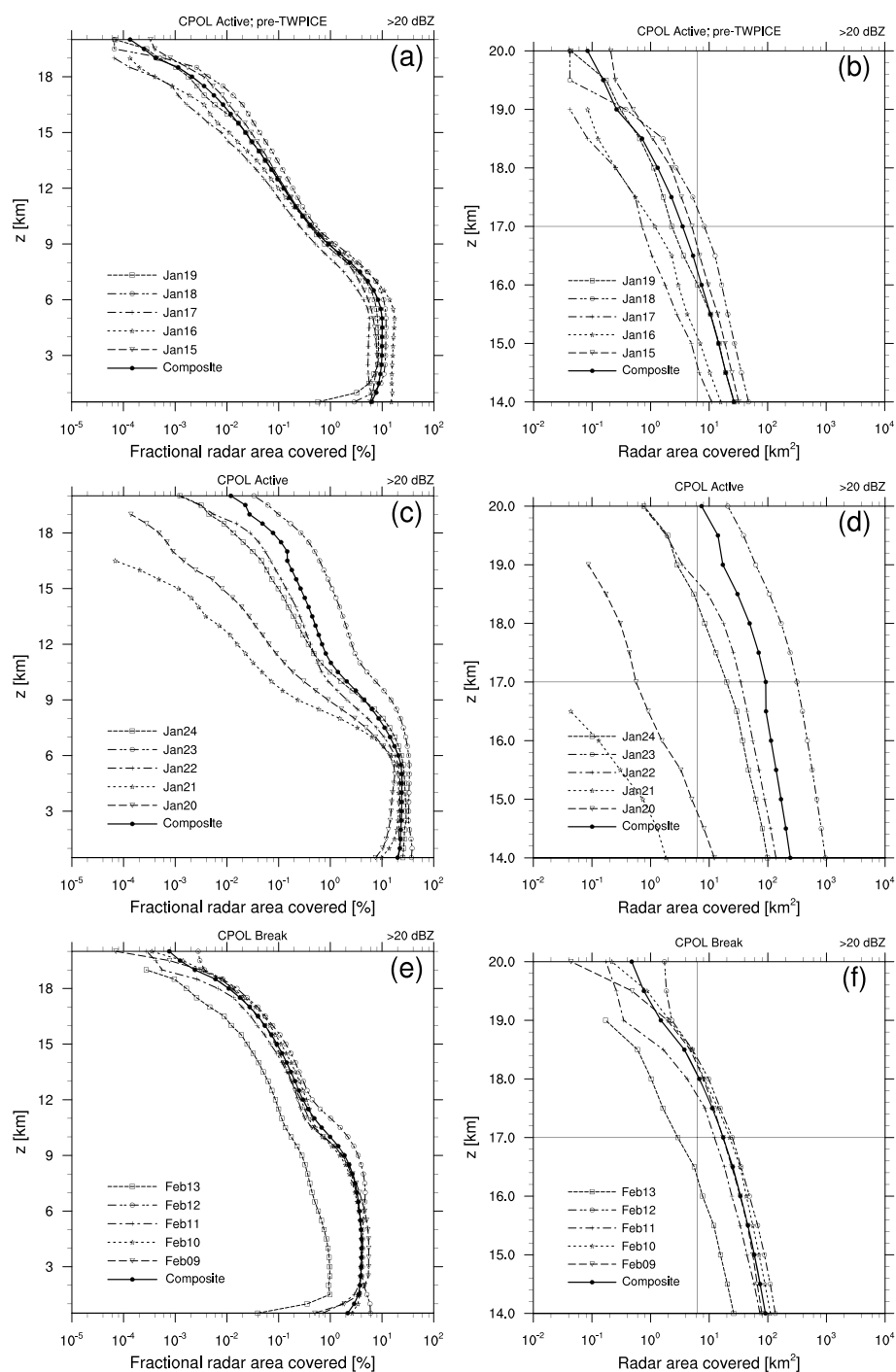


Figure 7. Fractional coverage (%) and equivalent radar area (km^2) covered by >20 dBZ echoes between 14 and 20 km for (a and b) 15–19 January, (c and d) 20–24 January, and (e and f) 09–13 February. The vertical line denotes the time-mean area covered if C-POL only detected a single 20 dBZ pixel (6.25 km^2) at that level every 10 min. The horizontal line denotes the approximate height of the mean cold-point tropopause during TWP-ICE defined in Figure 5.

monsoonal convection is less intense and detrains slightly lower than the more severe break period storms, corroborating previous studies [e.g., May and Ballinger, 2007; May et al., 2012].

Figure 7 presents fractional coverage profiles for echoes >20 dBZ for the pre-TWP-ICE period of 15–19 January (Figure 7a), the TWP-ICE active monsoon (Figure 7c), and the break period (Figure 7e). The equivalent overshooting area (in square kilometers) for altitudes ranging from 14 to 20 km are correspondingly shown in Figures 7b, 7d, and 7f. Daily means are plotted along with the composite for each sampled period

(average of the daily means). A vertical line denoting the area of a single 20 dBZ pixel (6.25 km^2) is also plotted in Figures 7b, 7d, and 7f to represent the mean overshooting area that would result if C-POL detected only one 20 dBZ pixel at that height level every 10 min. In this context, the line is considered an indirect reference for measuring the average frequency of overshoots occurring at various heights in the TTL.

Overall, Figure 7 reveals that overshooting convection around Darwin was very deep before and during TWP-ICE with $>20 \text{ dBZ}$ echoes extending throughout the entire TTL and reaching 20 km on most days. But there are differences. Notably, more variance is seen among the daily mean profiles before and during TWP-ICE (Figures 7a–7d) than during the break period (Figure 7e and 7f). Most profiles during the break phase tend to cluster around the composite. The exception occurred on 13 February, when areas $> 20 \text{ dBZ}$ are almost an order of magnitude less. This is in stark contrast to the considerable day-to-day variability seen above 6 km and particularly in the TTL during the TWP-ICE active phase (Figures 7c and 7d). Note that apart from 22 to 24 January, smaller mean overshooting areas are generally seen for the active period storms, both before and during TWP-ICE (Figures 7b and 7d) compared to the break period (Figure 7f). Overshooting storms during 15–19 January also infrequently penetrated past the height of the mean cold-point tropopause as inferred from daily mean overshooting area values that are smaller than one overshoot pixel (Figure 7b). During the observed break phase, storms tend to overshoot the mean tropopause almost daily and the composite area covered by reflectivities $> 20 \text{ dBZ}$ consistently range from about 100 km^2 (at 14 km) to around 10 km^2 (at 18 km) in the TTL (Figure 7f). This suggests that on average, overshooting cores from storms in the break period tend to be of similar size and magnitude from day to day.

The relative infrequency of overshoots seen for the active monsoon regime highlights the substantial influence exerted by the large MCS episode, such that the composite area of $>20 \text{ dBZ}$ pixels for the TWP-ICE active phase exceeded the break period profile by almost an order of magnitude above 17 km. This suggests that if the enhanced profile for 23 January was removed (as an outlier), the mean overshooting area during the sampled TWP-ICE active regime would more closely resemble values typical of active monsoonal convection exhibited by the pre-TWP-ICE period. Statistically, it is known from previous studies that convection during the active monsoon is generally weaker and intense overshooting cells are not as frequent. However, some storms can and do reach the level of the cold-point tropopause at around 17 km but not necessarily penetrating past it [May and Ballinger, 2007].

4. Observational Biases

So far, we have highlighted that properties of overshooting storms differ between the two large-scale regimes observed during TWP-ICE. Yet given the observational constraints of C-POL mentioned earlier, the issue of bias remains for statistics derived from the gridded product, especially for the TTL. These uncertainties undermine any ground-based estimate of total water input into the TTL by convective overshoots during TWP-ICE.

In this section, we attempt to estimate the bias in C-POL observations of the TTL during the two main convective regimes, using realistic cloud-system resolving WRF simulations performed for the same periods. These simulations were conducted with the Advanced Research WRF model version 3.1.1 [Skamarock *et al.*, 2008]. Simulated reflectivity fields derived from model data were then sampled using an algorithm that mimics the 3-D volumetric scan of the C-POL radar. The approach here is an abridged observing system simulation experiment (OSSE) [e.g., Arnold and Dey, 1986; Atlas, 1997]. In an OSSE framework, very high resolution simulations are taken as proxy for describing the “true” or “nature” state of the atmosphere with synthetic observations retrieved in a manner analogous to how real observations are made. Comparisons between the gridded synthetic retrievals and the original model reflectivities allow estimation of the observational biases.

4.1. WRF Model Simulations

For the monsoon break period, the 5 day model output reported by Caine *et al.* [2013] was used. It covers the period between 1200 UTC on 8 February and 1200 UTC on 13 February 2006. Using the same one-way nested four-domain configuration (Figure 8) and model setup (Tables 1a and 1b), a corresponding 5 day simulation of the active monsoon phase during TWP-ICE was performed for the period between 1200 UTC on 19 January and 1200 UTC on 24 January 2006. The first 12 h of these simulations are regarded as model spin-up and excluded from the analysis. As in Caine *et al.* [2013], the European Centre for Medium-Range

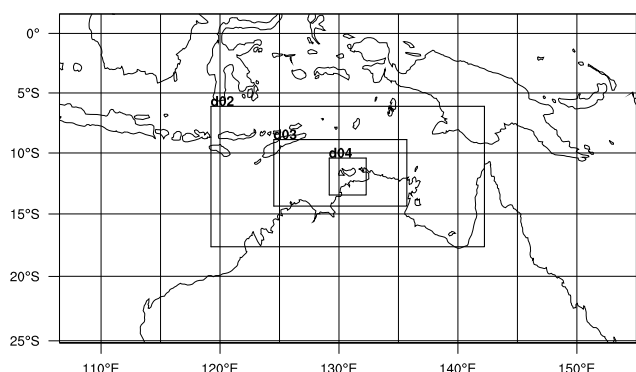


Figure 8. One-way nested four-domain configuration used for the TWP-ICE active and break periods WRF simulations.

Weather Forecasts Interim Reanalysis data [Dee *et al.*, 2011] are used for the initial and boundary conditions for consistency between the two periods. Note that the dimensions of the innermost cloud-system resolving domain (d04) were chosen to encompass the C-POL radar coverage, centered at Gunn Point (c.f. Figure 3). The time step used for the outermost domain is 90 s; the inner child domains have a nest-to-parent time step ratio of 3:1. All simulations used the Thompson microphysics scheme [Thompson *et al.*, 2008], with a slight modification described in Hassim and Lane [2010] to better account for the very cold TTL temperatures.

4.2. Baseline Reflectivities and Synthetic Radar Sampling

Gridded model reflectivity fields are constructed using 10 min output data from domain d04. The reflectivity is calculated from model microphysical variables using the forward conversion algorithm described in Caine *et al.* [2013]. The values calculated are assumed to be the baseline or absolute reflectivities (in dBZ) that would be measured, grid point by grid point, if the simulated radar was able to perform a perfect scan of the model domain without any gaps in coverage, signal degradation, or beam effects. We denote these values henceforth as “model-truth.”

Synthetic observations are produced by running the radar sampling algorithm described in the appendix on every model-truth reflectivity field from domain d04. The virtual radar is positioned at the center of the domain to replicate the location of the C-POL radar at Gunn Point. A 360° geometric “scan” of the model grid points is then conducted, following the C-POL strategy during TWP-ICE and accounting for the finite beam width of the radar. Hassim [2012] describes the development and testing of the radar emulation algorithm in further detail.

Volumetric data from the synthetic sampling are then interpolated onto a 3-D Cartesian grid with dimensions matching that of the gridded C-POL reflectivity product described earlier. The interpolation onto constant height levels uses the same SPRINT algorithm that produces the standard gridded C-POL product and is described by Mohr and Vaughan [1979]. Subsequent analyses are done using this final cartesianized radar product, along with the model-truth counterparts. Note that matching “truth” products are obtained by directly interpolating the original d04 gridded reflectivities onto a 2.5 km (horizontal) × 0.5 km (vertical) grid to facilitate proper “like-for-like” comparisons with the derived synthetic product.

Table 1a. Overview of WRF Model Configuration Used to Simulate the Active Period Observed During TWP-ICE

Domain ^a	Grid Size	Horizontal Grid Spacing (km)	Cumulus Parameterizations	Microphysics Scheme
d01	160 × 90	33.75	Betts-Miller-Janjic	Thompson 6-class ^b
d02	223 × 115	11.25	Betts-Miller-Janjic	Thompson 6-class
d03	319 × 157	3.75	not used	Thompson 6-class
d04	244 × 244	1.25	not used	Thompson 6-class

^a64 vertical levels, 10 mb model top, and a 5 km uppermost implicit gravity wave damping layer throughout.

^bThompson *et al.* [2008], modified with Murphy and Koop [2005] saturation formulae to cater for the very cold TTL temperatures.

Table 1b. Packages for All Domains

Common Physics Packages for All Domains	
Longwave	Rapid Radiative Transfer Model
Shortwave	Goddard shortwave radiation scheme
Surface layer	Eta similarity
Land surface	Noah Land Surface model
Boundary layer	Mellor-Yamada-Janjic (2.5 level)

Figures 9a and 9b provide illustrative examples showing that WRF was able to simulate overshooting convection captured in real C-POL data (c.f. Figures 3 and 4). These include the Hector and coastal storms over the Tiwi Islands (Figure 9a) and also a continental squall line typical of the break period (Figure 9b). Note that times chosen here are different to those C-POL examples shown earlier in Figures 3 and 4. It is expected that simulated storms will not be exact matches to observations, and timing differences demonstrate the inherent difficulty of modeling the atmosphere. Nevertheless, these examples show that WRF was able to simulate the different morphologies of convection typically experienced over the Darwin region during the monsoon season.

Examples of the synthetic observations at 14 km are presented in Figures 9c and 9d, while differences between the synthetic and model-truth fields are shown in Figures 9e and 9f. These examples highlight some of the intensity and slight positioning errors associated with the geometrical constraints of radar sampling. Note that “ringed” artifacts are also reproduced in the synthetic imagery, much like in real C-POL gridded data seen earlier.

In the synthetic C-POL product, the horizontal size and intensity of the overshooting areas are mostly underestimated compared to model-truth. The extent of the surrounding stratiform regions are also underestimated, albeit to a lesser degree (e.g., Figure 9b). These errors are seen because high-reflectivity overshooting updraft cores are, by nature, much smaller in scale and occupy only a fraction of the volume scanned by the radar at these altitudes. They are also inherently difficult to observe due to their transient nature. Such attributes are independent of the convective regime in which they occur. On the other hand, the lower reflectivity (stratiform) portions of the storms are much broader in scale and are therefore less influenced by beam broadening, partial beam filling, and subsequent volume averaging.

There are, however, localized regions at the storm peripheries where the strength of the echoes are overestimated (Figure 9e and 9f). These overestimates occur where features are horizontally “smeared”, thus exaggerating the actual areal coverage and intensities at those locations. Hassim [2012] argues that such overestimations can be seen in the gridded reflectivity field when the observed storm portion is small compared to the overall radar volume or isolated (such that there are no other beam observations on either side) and that the storm is far away from the radar.

WRF was also able to simulate the major features of the strongest events as well the differences seen between the two convective regimes fairly well (Figures 10a–10d). Note, however, that WRF has a tendency to produce too much reflectivity aloft. Wang *et al.* [2009] and Caine *et al.* [2013] showed that this is because the Thompson microphysics scheme in WRF produces too much snow. There are also timing and development errors, e.g., the prolonged overshooting events on 22 January and 12 February were not modeled properly. These highlight the known challenges faced by mesoscale models when simulating tropical convection at cloud-system resolving resolutions. Recent studies have shown that WRF is capable of capturing the known differences in convective updraft strength between observed TWP-ICE regimes and reproduce the depth of midlevel convection during the suppressed monsoon phase [e.g., Wu *et al.*, 2009]. Caine *et al.* [2013] also showed that observed storm size distributions for the break period were reasonably well represented by WRF simulations using the Thompson microphysics scheme. However, Wapler *et al.* [2010] concluded that for WRF to reproduce the observed statistics of rainfall in each TWP-ICE phase reasonably well, the characteristic mesoscale flow for that regime needed to be modeled adequately.

Nonetheless, WRF, in our study, was able to capture the bulk and duration of the most intense overshooting activity during the passage of the MCS on 23 January. Overall, based on animated sequences of both

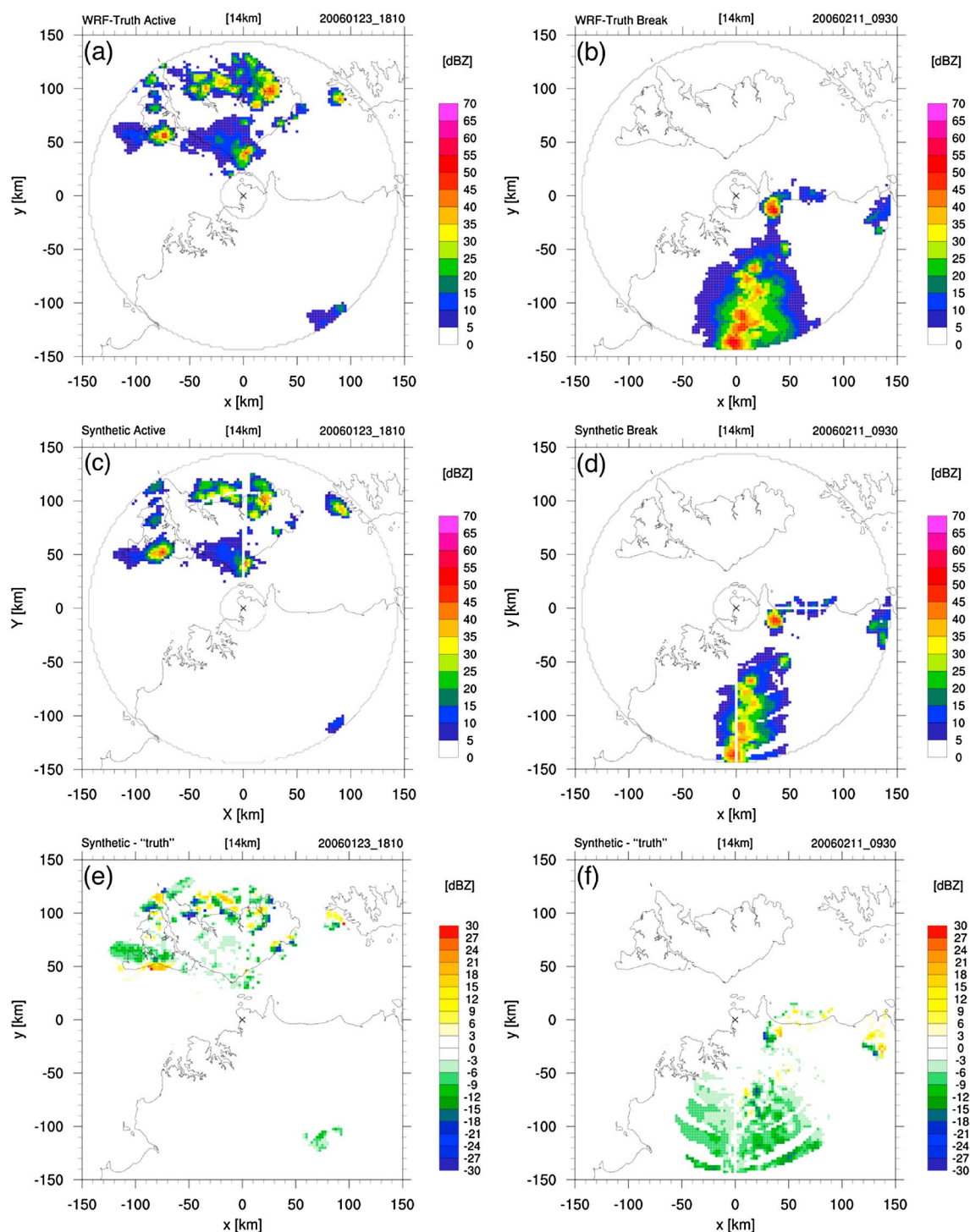


Figure 9. (a and b) Model-truth and (c and d) synthetic radar reflectivity at 14 km for a selected day in the active (Figures 9a and 9c) and break (Figures 9b and 9d) periods. The difference of Figures 9c minus 9a and 9d minus 9b are shown in Figures 9e and 9f, respectively. Times shown are in UTC.

simulated and real C-POL reflectivities at 14 km (not shown), the model simulations produce a fairly realistic representation of overshooting storms in terms of their spatial distribution from the virtual radar. For each TWP-ICE period, we found simulated overshooting storms propagating across the domain, much like those in the observed C-POL record. Simulated storms were therefore sampled at a range of distances from the virtual radar, just like in the real world, despite the timing and intensity errors.

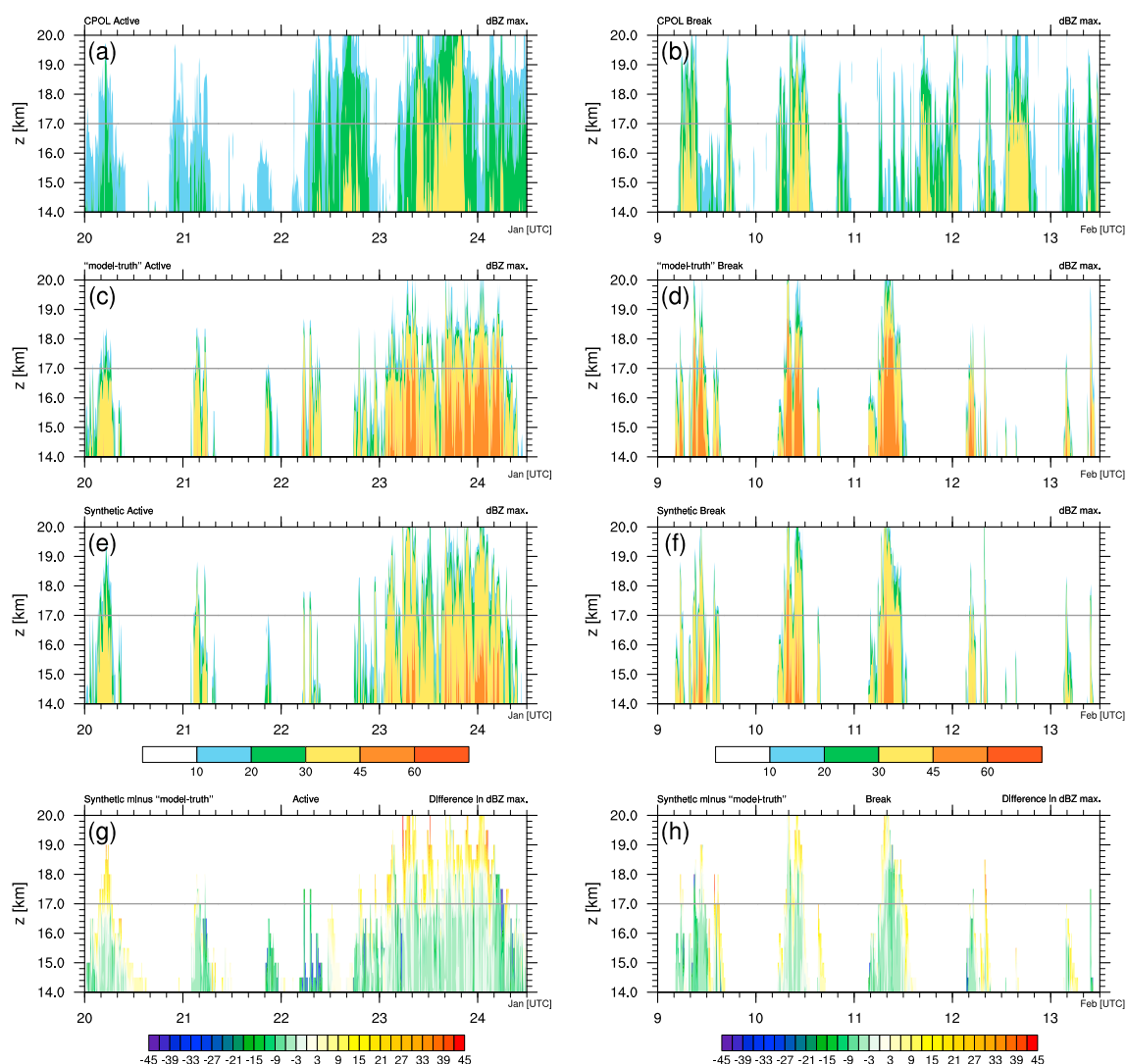


Figure 10. Maximum reflectivity (Z_{\max}) at 14–20 km during the (left) active and (right) break periods: (a and b) C-POL observations, (c and d) model-truth simulated by WRF, and (e and f) synthetic observations. (g and h) Differences in dBZ between synthetic observations and model-truth.

Results from the synthetic sampling for Z_{\max} are shown in Figures 10e and 10f and biases in Figures 10g and 10h. The errors in the synthetic data are mainly due to the radar's geometrical constraints, which are discussed in detail in Hassim [2012]. In brief, partial beam filling due to the broadening effect with range explains the reductions in actual intensity, since the reflectivity measured will be averaged over the entire measurement volume.

Conversely, considerable echo-top height “smearing” (i.e., exaggerating the true vertical extent of echoes measured) can occur when a portion of the overshooting storm is only just sampled by the bottom half of a beam. This is because echo heights are determined from the height of the beam axis. It can also occur when the interpolation onto constant height levels at high altitude is done over large vertical gaps between beam elevations. While this may explain the “stretched” vertical coverage of >30 dBZ echoes at the expense of the >45 dBZ echoes in Figures 10e and 10f compared to Figures 10c and 10d, it must be noted that the balance between horizontal and vertical uncertainties arising from the cartesian interpolation procedure used in this study is not entirely obvious. An example of echo-top height “smearing” can be seen on 20 January between 0400 and 0600 UTC (Figure 10e). Maximum echo-top (and storm) heights in our cases are only underestimated when storms are close to the radar or within the radar's cone of silence.

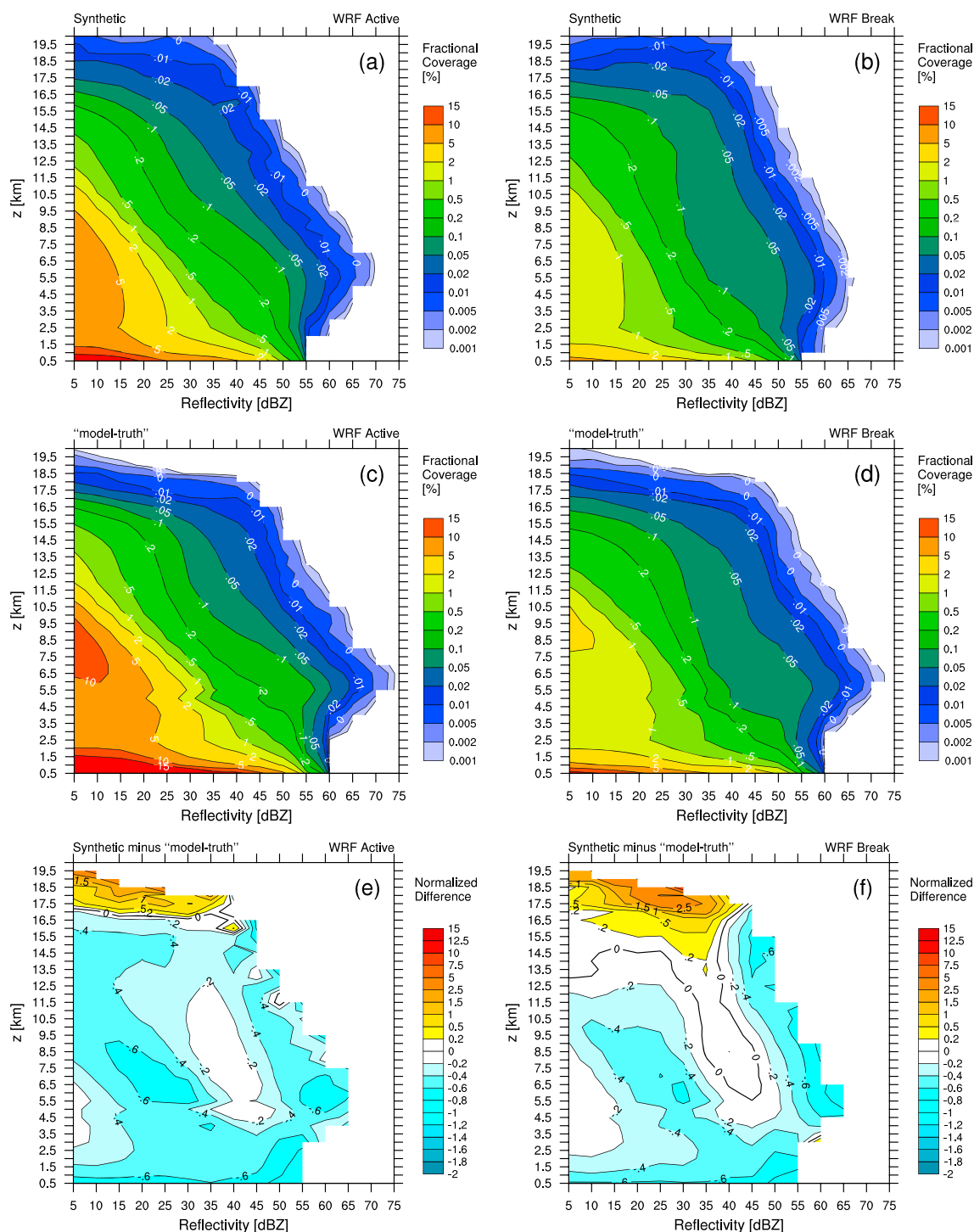


Figure 11. Composite CCADs derived from (a and b) synthetic observations, (c and d) model-truth, and (e and f) the normalized difference between them for (left) active and (right) break phases, respectively. Differences have been normalized with respect to model-truth.

4.3. Bias Assessment

Bulk statistics from the synthetic observations are shown in Figures 11a, 11b, 12a, and 12b. These show the composite CCADs and profiles of mean overshooting area in the TTL, respectively. Also shown are corresponding statistics derived from model-truth; Figure 11 also presents plots of normalized differences (Figures 11e and 11f). These plots highlight that the main regions of significant bias in the reflectivity area statistics occur in the TTL and especially above 17.5 km. At these levels, the relative proportion of radar area

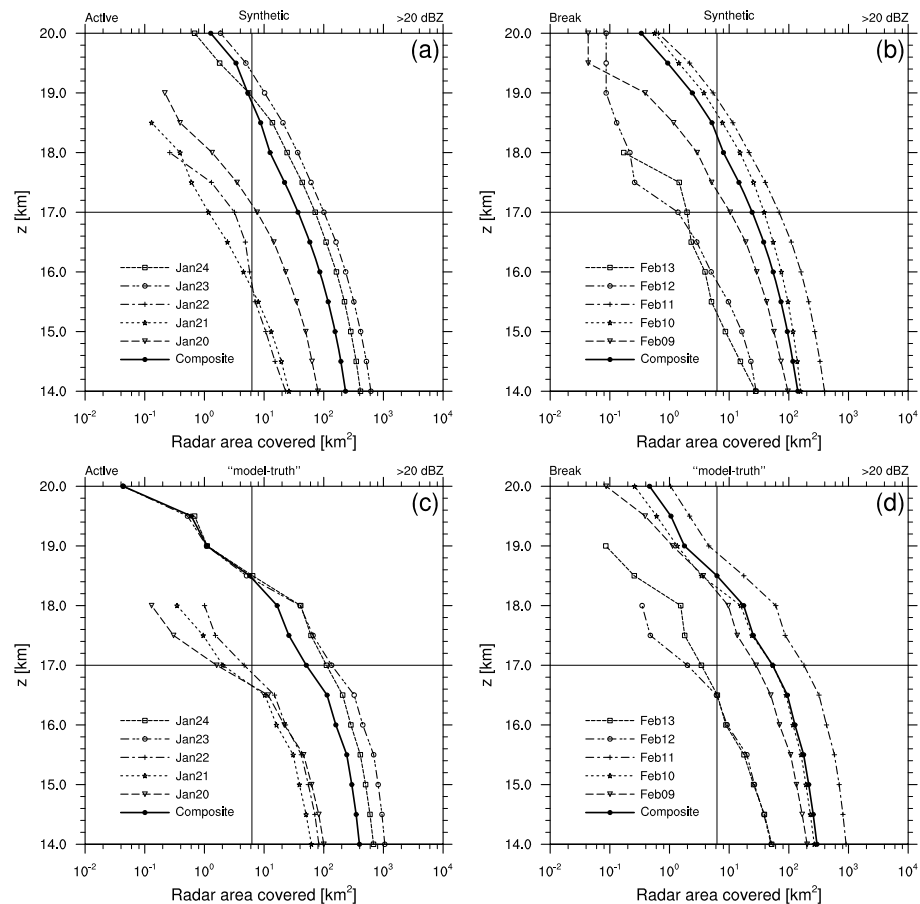


Figure 12. Daily mean and composite radar area (km^2) covered by >20 dBZ echoes between 14 and 20 km, for the TWP-ICE active and break periods, respectively. (a and b) Synthetic observations. (c and d) Model-truth. The vertical line denotes the time-mean area covered if only detected a single 20 dBZ pixel (6.25 km^2) was detected at that level every 10 min. The horizontal line denotes the approximate height of the mean cold-point tropopause during TWP-ICE defined in Figure 5.

covered by 20–35 dBZ echoes have been exaggerated. These differences are consistent across both TWP-ICE periods. Interestingly, the detection of echoes up to 20 km in Figures 11a and 11b (but shown in Figures 11e and 11f to be an observational bias) coincides well to that seen earlier in the C-POL statistics (c.f. Figure 6).

Note that below the TTL (14 km), virtual radar sampling has underestimated the areas covered by echoes including those normally associated with convective cores, i.e., 45–65 dBZ echoes, between 4.5 and 17.5 km (Figures 11e and 11f). The radar has also diminished the model-truth Z_{max} areal frequency around 6 km for both periods (Figures 11e and 11f). This is due to horizontal “smearing” from beam filling and volume averaging, which reduces the absolute reflectivity measured.

Figures 12a and 12b show that the mean 20 dBZ echo heights have also been vertically “smeared” in the synthetic observations, with increases of 1–2 km on 20–21 January and 12 February but a decrease of 1 km on 13 February, compared to model-truth (Figures 12c and 12d). However, these errors were registered on days in which overshooting events above 16.5 km were relatively infrequent. In fact, model-truth profiles for both periods suggest that overshooting above 18.5 km was, on average, a relatively rare occurrence during the two simulated TWP-ICE regimes. Despite this, we cannot exclude the possibility that the rarity of overshooting tops above 18.5 km could also be a model bias.

Height-resolved biases in the TWP-ICE active and break periods are further identified in Figures 13 and 14, respectively. These show separate profiles of the daily mean fractional coverage above 20 dBZ as derived from model-truth and the synthetic radar sampling. Significantly, the plots indicate that the virtual radar

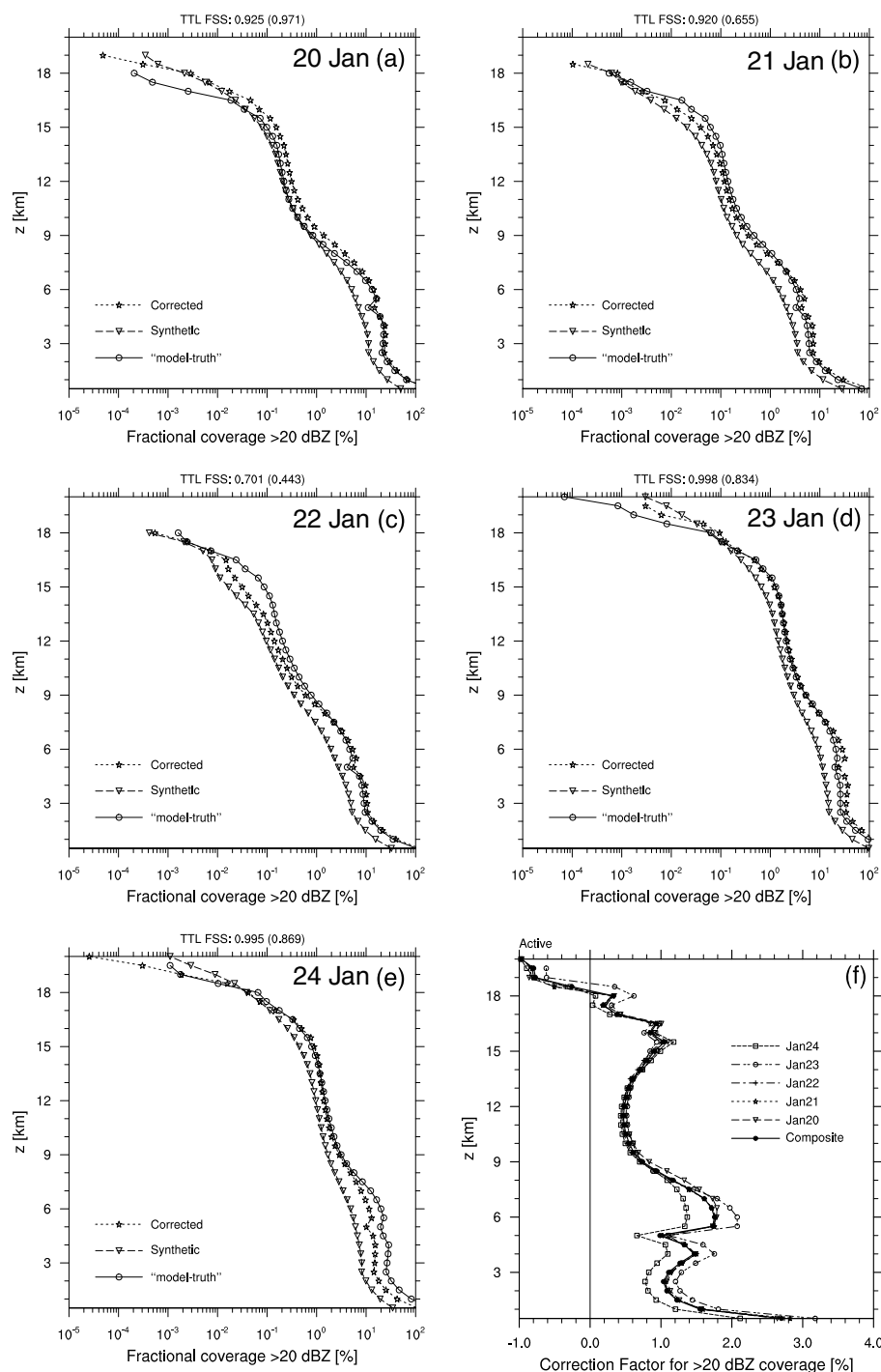


Figure 13. (a–e) Profiles of daily mean fractional coverage above 20 dBZ (%) for model-truth, synthetic, and corrected observations for the TWP-ICE active period. (f) The daily correction factors along with the overall correction factor for the regime. TTL fractions skill scores (TTL FSS) computed using only the 14–20 km levels are shown at the top of the daily plots. The number in the parentheses is the TTL FSS of the noncorrected profile derived from synthetic sampling.

has persistently underestimated the “true” mean fractional area covered by reflectivities >20 dBZ between 0.5 and 17 km on every single day. However, they also reveal that the radar exaggerated the >20 dBZ fractional coverage for heights above 17 km on 3 days (20, 23, and 24 January) during the active period (Figures 13a, 13d, and 13e). In contrast, it only overestimated the areal coverage on 10 February (Figure 14b) but underestimated it on other break period days for those levels (Figures 14a and 14c–14e).

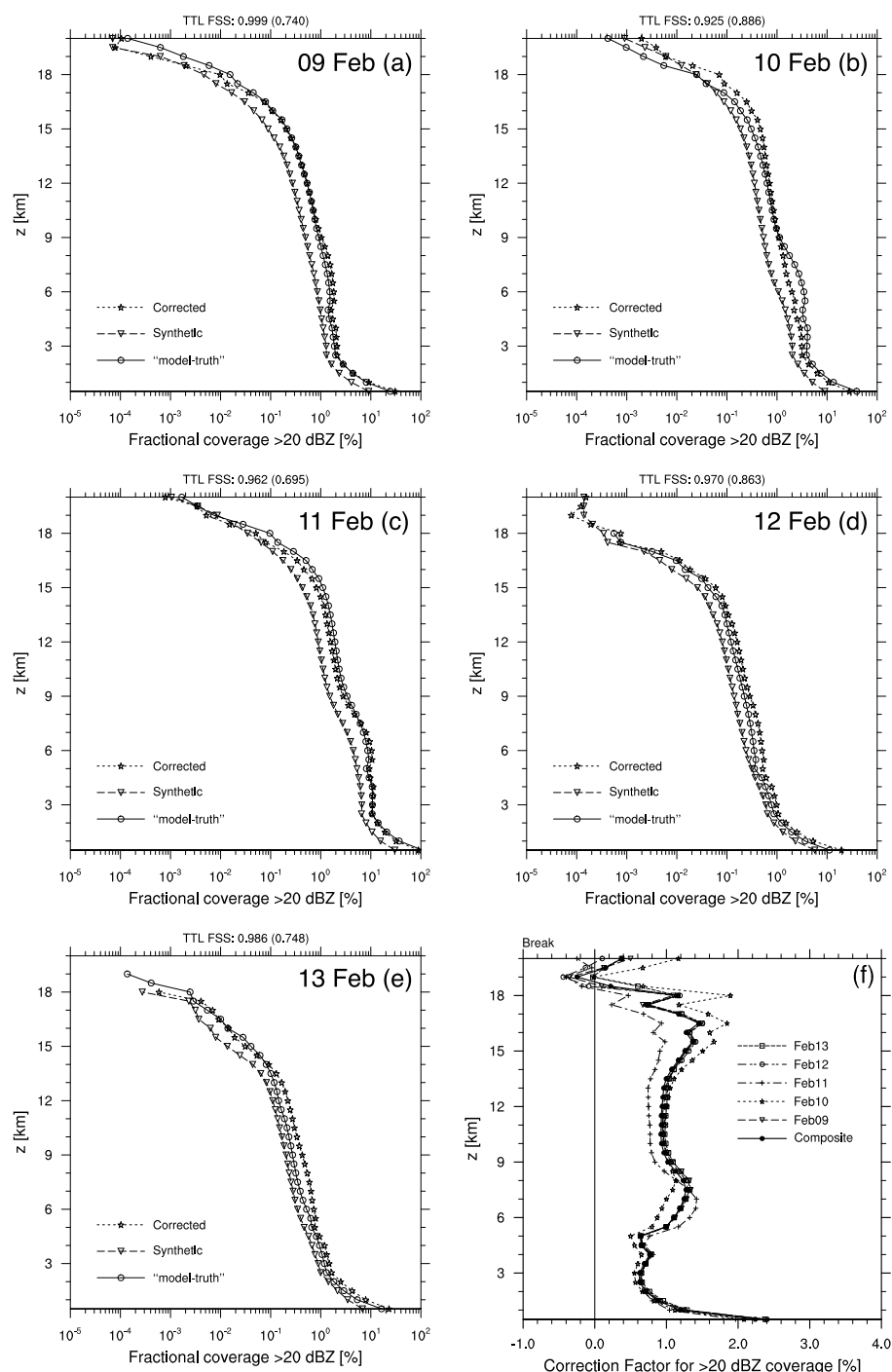


Figure 14. As in Figure 13 but for the break period between 9 and 13 February 2006.

5. Bias Correction

The preceding analysis demonstrates that radar-derived reflectivity products suffer from inherent uncertainties due to sampling and geometric constraints. These are largest in the TTL and affect the overshooting area statistic. While the errors seem small, correcting them is important so that better estimates of mean overshooting area and depth can be made to help constrain the daily upward transport of water into the TTL by convective overshoots. Of course, not all of the overshooting material is detrained. Most will just

descend back to lower levels in the TTL, and the net amount will depend on how much mixing occurs during the overshoot duration.

Nevertheless, for our purpose, we propose a simple altitude-dependent correction to rectify the daily mean overshooting area “observed” at a given level during each modeled period. The correction scheme is given below by

$$A_c(z) = A_s(z) + \left(\frac{\overline{\{A_r(z)\}}}{\overline{\{A_s(z)\}}} - 1 \right) \times A_s(z) \quad (1)$$

where A_c is the *corrected* overshooting area at height z , A_s is the overshooting area derived from synthetic observations, and A_r is the overshooting area obtained from model-truth reflectivity fields. The overbars indicate a composite taken over the set of all daily mean values, i.e., $\{A_r\}$ and $\{A_s\}$, but excludes the day that is being corrected. In other words, each day is being corrected by the average of all other days to ensure an independent set. Thus, the term in the square brackets represents the *composite* correction factor needed to amend the “observed” daily mean overshooting area at height z and is guided by the corresponding model-derived absolute value. The magnitude of the correction is simply a proportion of the initial “observed” value. The daily composite correction factors are then used to construct an overall correction factor for the simulated period such that each regime has its own independent correction.

Figures 13 and 14 also present profiles of the corrected daily mean fractional coverage for reflectivities >20 dBZ in each period, respectively. The composite correction factor for each day and the overall correction factor for the TWP-ICE active and break phases are shown in Figures 13f and 14f, respectively.

To quantitatively assess the effectiveness of the correction scheme, a fractions skill score (FSS) is calculated following *May and Lane* [2009], who adapted the method described in *Roberts and Lean* [2008]. The FSS is given by

$$FSS = 1 - \frac{FBS}{\frac{1}{N} \left[\sum_{j=1}^N m_j^2 + \sum_{j=1}^N o_j^2 \right]} \quad (2)$$

where m_j is the fractional coverage from model-truth, o_j is the “observed” fractional coverage, N is the total number of reflectivity bin samples in each gridded data set, and

$$FBS = \frac{1}{N} \sum_{j=1}^N (m_j - o_j)^2 \quad (3)$$

is the fractions Brier skill score in which fractions are compared [*May and Lane*, 2009].

The FSS represents an integrated measure of the net overall agreement between two probability distribution functions. In our case, it measures how accurate the corrected synthetic “observation” matches the corresponding model-truth statistic. The FSS is a variation of the Brier score function that has been normalized by the worst possible score achievable (i.e., when the average squared deviations are maximized). It covers a range from 0 to 1, where 0 is a complete mismatch while 1 is perfect.

Based on their respective TTL fractions skill scores (TTL FSS)—calculated using only TTL levels—all but one of the corrected profiles exhibit excellent agreement with their corresponding model-truth (TTL FSS >0.9). In particular, corrected profiles for 23–24 January (Figures 13d and 13e), along with that for 9 February (Figure 14a), deliver almost exact reproductions of their respective “model-truths,” particularly in the TTL region below 18.5 km as denoted by TTL FSS scores of ≥ 0.99 . In general, revised skill scores in excess of 0.92 were achieved on four out of five active period days, and despite having a revised skill score of only 0.70, the proportional skill improvement for 22 January was actually the highest among all the days, at $\sim 58.2\%$. All corrected profiles for the break period achieved revised skill scores greater than 0.92; four out of five of those profiles obtained TTL FSS scores greater than 0.96. Quantitatively, these high FSS values highlight the considerable accuracy of the proposed correction scheme in correcting the biases from virtual radar observations. This raises the possibility of using the respective overall correction factors to rectify the mean areal statistics calculated from real C-POL measurements for each TWP-ICE period.

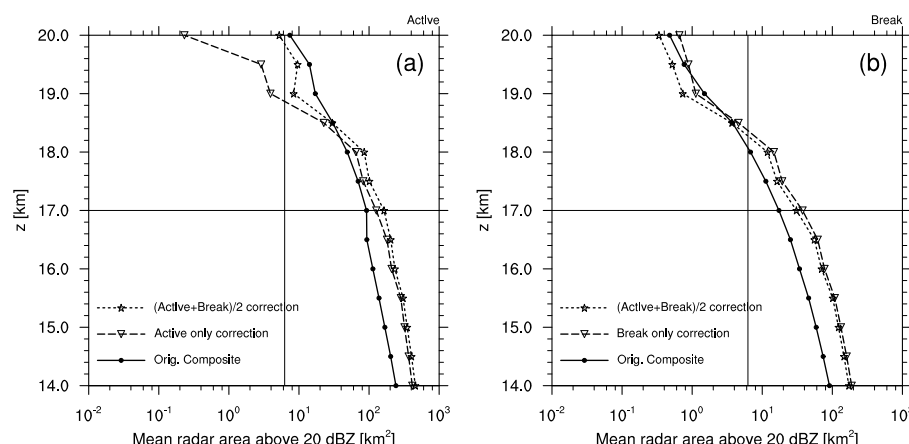


Figure 15. Corrected C-POL profiles of composite overshooting area (km^2) in the TTL: (a) TWP-ICE active monsoon phase and (b) TWP-ICE break period, for different overall correction factors. The vertical line denotes the mean overshooting area that would result if only a single 6.25 km^2 pixel overshoot was observed anywhere within the radar area at that level.

5.1. Correcting the C-POL Overshooting Area Statistic

Our application of the shortened OSSE framework in section 4.2 has highlighted the likely extent of biases resulting from ground-based radar sampling. Given the skill of the proposed correction scheme, the overall correction factor for each synthetically sampled modeled period are now applied to the composite overshooting area statistic derived earlier from real C-POL observations (see Figures 7d and 7f). We note that the WRF model exhibits some weaknesses in reproducing detailed aspects of the C-POL observations. These include the simulation of larger reflectivity values than what was observed over comparable altitudes and the timing of some convective overshooting features. However, applying the synthetically derived corrections to C-POL data is still useful because the overall bias of overestimation and underestimation is likely robust.

Revised C-POL profiles of composite overshooting area in the TTL are presented in Figures 15a and 15b for the two main TWP-ICE convective regimes, respectively. Two separate corrected profiles are drawn, along with the original C-POL profiles previously depicted in Figures 7d and 7f. The first corrected profile comes from independently applying the respective overall correction factor for each TWP-ICE phase, shown earlier in Figures 13f and 14f. The second uses the *average* of the two overall correction factors (i.e., the (Active+Break)/2 correction). In general, the resultant corrected profiles display increases in composite overshooting area at every height level below 18.5 km, while reductions are seen above 18.5 km (Figures 15a and 15b).

Differences between the original and corrected C-POL values between 14 and 18 km are substantial (Table 2). These range from ~ 180 to $\sim 100 \text{ km}^2$ at the 14 km height level and ~ 14 and $\sim 8 \text{ km}^2$ at 18 km for the TWP-ICE active and break periods, respectively. Both corrected profiles show increases in mean overshooting area below 18 km and reductions above 18 km, but the changes are relatively more so for the active monsoon phase. This suggests that apart from the atypical 23 January MCS day, overshooting convection reaching 19–20 km high are rather infrequent events during the active monsoon regime. Overshoot statistics for the active period are therefore more prone to bias at those heights due to the small and transient scale of convective overshoots. The largest magnitude gains are seen for the TWP-ICE active monsoon regime when its individual overall correction factor was applied. In contrast, the biggest percentage gains were found for the break period correction, with corrected overshooting areas being more than twice the size of the original composite values up to 18 km. When the average of the two overall correction factors was applied, identical percentage changes were obtained for all altitudes across both regimes. The use of this average can be interpreted as the generalized correction needed to rectify the observed horizontal area covered by overshooting updrafts at various heights in the TTL under mean environmental conditions during TWP-ICE.

It is important to note, however, how biases in the simulations can impact the correction factor for each regime. Indeed, the location, number, and intensity of overshooting storms might be poorly modeled on particular days. Of these possible errors, the location of storms relative to the radar could have the most

Table 2. Summary of the Changes in Composite Overshooting Area (Shown at 1 km Intervals) After Profile Corrections Seen in Figure 15^a

Height Level	Original Area (km ²)	Active		
		Difference (km ²) ^b	Active Only (%) ^c	(Active+Break)/2 (%) ^d
14 km	257.4	183.4	71.3	89.2
15 km	179.5	163.4	91.0	108.3
16 km	121.6	103.5	85.1	106.3
17 km	79.6	30.1	37.8	77.4
18 km	42.4	14.0	33.0	74.6
19 km	14.9	−11.5	−77.2	−50.9
20 km	4.8	−4.7	−97.9	−29.5
Height Level	Original Area (km ²)	Break		
		Difference (km ²) ^b	Break Only (%) ^c	(Active+Break)/2 (%) ^d
14 km	91.0	97.6	107.3	89.2
15 km	58.8	73.9	125.7	108.3
16 km	34.0	43.4	127.6	106.3
17 km	17.3	20.3	117.3	77.4
18 km	6.8	7.9	116.2	74.6
19 km	1.5	−0.4	−26.7	−50.9
20 km	0.5	0.2	40.0	−29.5

^aThe difference is calculated as “corrected minus original.”

^bChange in magnitude when rectified with either the Active or Break overall correction factor.

^cPercent change with respect to original area when corrected with either the Active or Break overall correction factor only.

^dPercent change with respect to original area when corrected with the *average* between the Active and Break overall correction factors.

effect. If the model disproportionately simulated overshooting storms either too close (such that they only appear within the radar’s cone of silence) or too far away during a particular regime (e.g., near the extreme peripheries of the radar domain), smaller overshooting areas would be observed by the virtual radar, on average. A larger overall correction factor would then result based on equation (1).

Nonetheless, the bias correction would still be robust regardless of regime because WRF, in this study, was able to simulate the convective characteristics in different large-scale conditions reasonably well. Furthermore, an animated sequence of C-POL imagery at 3 km (not shown) revealed that WRF simulated storms propagating across the radar domain at various locations; overshoots in the TTL were therefore sampled over a range of distances.

In any case, the corrected mean overshooting area with height serve to better constrain the total convective transport of water vapor and ice mass into the TTL by overshooting events during each TWP-ICE regime. Notably, the magnitudes of the rectified values at 17 km are consistent with the known size of overshooting tops penetrating the tropopause (≤ 15 km in diameter or ≤ 177 km²) as analyzed from visible and infrared satellite imagery over continental United States at both 1 km and 4 km resolutions [Bedka *et al.*, 2010; Dworak *et al.*, 2012]. This is an encouraging result and shows that ground-based radars like C-POL can resolve penetrating convection. This also suggests that the average horizontal size of cloud overshoots is similar regardless of region, at least in the vicinity of the tropopause. Our methodology of using high-resolution WRF runs and ground-based radar can therefore complement space-borne radar observations with similar fields of view, namely, CloudSat (1.8 km along \times 1.4 km across track) [Stephens *et al.*, 2008] and the Tropical Rainfall Measuring Mission precipitation radar (TRMM PR, ~ 4.3 km resolution at nadir) [Kummerow *et al.*, 1998]. For the TRMM PR, this equates to an effective pixel size of ~ 20.35 km² [Liu and Zipser, 2005], which is actually coarser than the pixel resolution of the C-POL radar product used in our study to characterize overshoot properties (c.f. 6.25 km²). Given enough overhead passes over Darwin to overcome the poor temporal sampling of both satellites, a useful validation exercise would certainly be to compare overshooting area detections between the various platforms, similar to that conducted

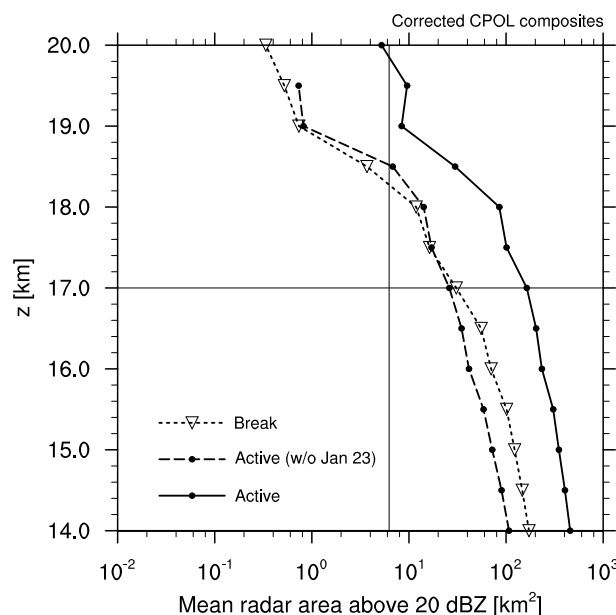


Figure 16. Corrected C-POL mean overshooting area (km^2) in the TTL, rectified with the *average* of the two overall correction factors for each regime, i.e., $(\text{Active} + \text{Break})/2$ generalized correction.

by Liu *et al.* [2010b] between the millimeter-wavelength cloud radar facility in Darwin and CloudSat observations. However, it is already promising to note that the average corrected value of mean overshooting area observed by C-POL at 14 km ($\sim 200 \text{ km}^2$) compare well with the global mean overshooting area diagnosed from TRMM PR data for the same height level ($\sim 244 \text{ km}^2$; Liu and Zipser [2005]).

For emphasis, values of composite overshooting area from C-POL that have been corrected by the generalized correction factor (i.e., the $(\text{Active} + \text{Break})/2$ correction) are replotted in Figure 16 for each TWP-ICE period. A third profile is also drawn, which shows the corrected composite values for the TWP-ICE active phase with the influence of the 23 January MCS day removed (Figure 16, long dash-dotted line). Remarkably, the generalized results indicate that more water was transported into the TTL by overshooting convection during the active monsoon phase of TWP-ICE than in the break period (Figure 16, dotted solid line). However, when the MCS day was excluded, the revised values of composite overshooting area for the active monsoon regime are only marginally lesser than those corrected for the break period up to the mean tropical cold point ($\sim 17 \text{ km}$). The dashed profiles in Figure 16 therefore represent the characteristic mean overshooting area with height for the two main convective regimes of a typical monsoon season over Darwin. Given that updraft speeds are greater in the break period than during the active monsoon, especially in the upper troposphere [Wu *et al.*, 2009], this suggests that overshooting convection during the break period would typically transport more water into the TTL, on average. Note that the overshooting areal trend in Figure 16 is slightly opposite above 17.5 km, with the active period profile exceeding that of the break period. This implies that the occurrence of the deepest cells is similar during both periods, although the area statistics above 18 km are likely not significant. That being said, there can be significant mass flux into the lower stratosphere during singular large overshooting events.

Nevertheless, the marginal difference between the corrected profiles when the MCS day is removed is somewhat surprising. However, it represents an important finding that reflects the relative proportion of overshooting storms that typically occur within each deep convective regime. Storms during the break period are relatively more episodic but they are more intense and tend to overshoot when they occur. Conversely, there is relatively more convection during the active monsoon phase but less frequent overshoots from storms, typically. It is worth noting though that because of Darwin's location, the active period systems sampled during TWP-ICE are more coastal storms with a maritime influence rather than truly oceanic convection. In this regard, it remains to be seen whether our results are fully applicable to other deep convective systems that develop solely over water. Indeed, Liu *et al.* [2007] showed using TRMM data that there

are distinct differences in updraft sizes (based on the area of 20 dBZ echoes reaching 14 km) between land and purely oceanic systems that reach the tropopause.

6. Conclusions

In this study, overshooting convection during the Tropical Warm Pool International Cloud Experiment (TWP-ICE) in Darwin, Australia, been analyzed using the gridded C-POL radar data set. The aim is to characterize the statistical properties of overshooting events in the tropical tropopause layer (TTL) and their variability between the active and break periods of the monsoon. An additional objective is to estimate and correct for the biases in mean overshooting area with height. This was done using guidance from synthetic radar observations, which were retrieved from cloud-system resolving WRF simulations using a radar sampling emulation algorithm. These simulations were regarded as proxy for the true atmosphere during the two TWP-ICE periods as part of an abridged observing system simulation experiment (OSSE). The virtual radar sampling mimicked the effective beam width and scanning strategy (and therefore the geometrical constraints) of the C-POL radar during the field campaign.

Observations show that very deep convection reached the TTL daily during both regimes sampled by TWP-ICE, with >20 dBZ echoes commonly seen up to 18 km. However, overshooting storms were more intense during the break period than in the active monsoon regime (as expected) when the atypical influence of the MCS day was removed from the statistics. Severe break period storms also showed lesser diurnal variability in terms of mean overshooting area with height. This finding emphasizes the reliable occurrence of high-reaching overshooting convection during the monsoon break period and corroborates previous studies for the Darwin region [e.g., *Vallgren*, 2006; *May and Ballinger*, 2007]. However, the frequency of occurrence of the deepest cells (i.e., those that reach above 18 km) appear to be similar between the break and active periods, although it must be stated that statistics above 18 km are likely to be not significant.

C-POL observations are shown to contain some considerable biases in convective core intensities, mean overshooting area, and the erroneous assignment of echo-top heights on individual days. Synthetic observations from the emulated radar sampling—conducted as part of a shortened OSSE approach—showed that the radar has a tendency to overestimate 20 and 30 dBZ echo-top heights while underestimating the vertical extent of >45 dBZ echoes and the highest core intensities. The composite overshooting area in the TTL for each period is also underestimated, except for heights greater than 18 km, where it is exaggerated.

The areal biases are shown to be substantial with values ranging from $\sim 180 \text{ km}^2$ ($\sim 100 \text{ km}^2$) to $\sim 14 \text{ km}^2$ ($\sim 8 \text{ km}^2$) between 14 and 18 km for the active (break) period after corrections are made. However, relative differences between each regime are small when the strong MCS influence was removed. These corrected values are expected to increase any upscaling estimate of the amount of water vapor and ice mass transported into the TTL by convective overshoots during the monsoon season. It should be noted that statistics and the overall correction factors should ideally be derived over a much larger and longer synthetic data set that composites a number of similarly modeled convective regimes to build robustness. However, because of the heavy computational and time burden of such an undertaking, such an approach would require judicious selection of an appropriate number of regime days over several typical seasons.

Furthermore, our study did not investigate the distribution of overshooting area in relation to overall storm size for individual cells. Using TRMM PR data, *Liu and Zipser* [2005] has shown that intense thunderstorms around Darwin have a large overshooting area proportion with respect to storm size (>40 %) during the austral summer. Presumably, data from space-borne radars like TRMM PR and CloudSat are less prone to the sampling artifacts seen in ground-based radar products at high levels but are likely to suffer from their own biases. A future study of convective overshooting properties between corrected C-POL data and statistics from TRMM and/or CloudSat for the Darwin region is recommended for cross-validation purposes.

Appendix A: Synthetic Radar Algorithm

A1. Beam Geometry

The algorithm used mimics the 3-D beam geometry of the C-POL radar and its scanning strategy during TWP-ICE. It accounts for both the bending of the beam due to the Earth's curvature at far distances and the beam broadening effect with range. The algorithm assumes that the beam spread is limited to the angular

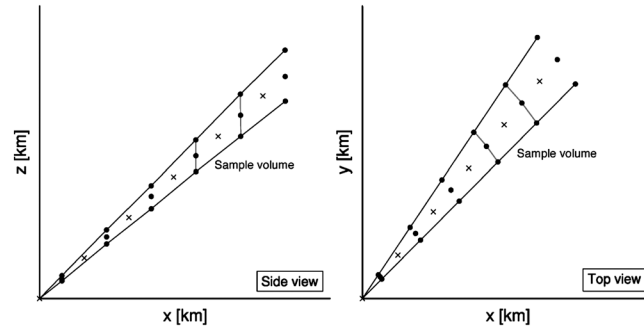


Figure A1. Schematic showing the side and top views of the cartesianized beam geometry. Black dots denote interpolation points. The range gate position is denoted by the “cross” along the central beam axis of a given elevation. A sample volume is constructed by joining the black dots surrounding the central “cross” across the side and top. See Appendix A for details.

beam width of the radar (a fixed geometrical property of the system). Thus, the size of each measurement volume, V , (i.e., range bin) increases with distance according to the equation

$$V = hr^2\theta^2 \quad (\text{A1})$$

where h is the pulse width or *range resolution* (e.g., $1 \mu\text{s}$ times the speed of light, $3 \times 10^8 \text{ m s}^{-1}$), r is the distance travelled by the pulse from the radar (in metres), and θ is the beam width (in radians). For example, equation (A1) reveals that for a C-POL beam width of 1° and a pulse width of $1 \mu\text{s}$ (corresponding to a range resolution of 300 m), sample volume sizes at a range of 50, 100, and 150 km would approximately measure 0.22 km^3 , 0.91 km^3 , and 2.0 km^3 , respectively.

Geometrically, the height of the beam axis above ground level, assuming standard atmosphere refraction, is given by

$$z = \left(\sqrt{d^2 + (k_e r_e)^2 + 2dk_e r_e \sin(\theta)} \right) - k_e r_e \quad (\text{A2})$$

where z is the height of the beam axis (in metres) above radar level, d is the distance of each range gate from the radar along the beam axis (in metres), k_e is the refractive index of a standard atmosphere $\frac{4}{3}$, r_e is the effective radius of earth (in meters), and θ is the elevation angle (in radians). A complete 3-D description of the radar beam in cartesian space is thus given by

$$y = S \cos(\phi) \quad (\text{A3})$$

and

$$x = S \sin(\phi) \quad (\text{A4})$$

where ϕ is the azimuth angle and S is the *arc-distance* along the Earth’s surface given by

$$S = k_e r_e \arcsin \left(\frac{d \cos(\theta)}{(k_e r_e + z)} \right) \quad (\text{A5})$$

A2. Scanning of Model Space

To mimic the volumetric scan, the model space is surveyed through an iterative routine that treats every azimuth at each elevation as an individual vertical plane during a full rotation sweep. First, gridded model reflectivities contained within that azimuthal plane are bilinearly interpolated onto a series of cartesianized range gate positions (along the beam axis) given by the zx coordinate pairs obtained from equations (A2) and (A4). The 3-D horizontal (and vertical) beam spread with range are approximated by projecting cartesianized *beam edge lines* at half the effective beam width angle either side of the original azimuth (elevation) that describes the central axis. For an azimuthally scanning radar like C-POL, the effective beam width is wider in the azimuthal direction ($\sim 1.46^\circ$) than it is in the direction of the elevation angles (1°) as discussed by Blahak [2008]. The projection of these beam edges form sample volumes corresponding to the range gates along the central beam axis. A schematic showing the side (zx plane) and top (yx plane) views of a cartesianized sample volume is presented in Figure A1.

Subsequently, gridded model reflectivities are interpolated onto the 18 points of the sample volume. Consistent with the definition of the beam width as being the *half width* of the beam power, the magnitudes of interpolated reflectivities at the beam edges are halved (to approximate a weighting factor of 0.5); those along the central beam axis retain full interpolated magnitudes (weight of 1.0). Finally, the interpolated reflectivities are linearly averaged (first vertically and then horizontally) across the entire 3-D construct, including the value interpolated onto the central axis, to obtain the mean reflectivity for the corresponding sample volume.

This procedure represents a simplified form of volume averaging similar to that employed in the studies of Wood *et al.* [2009] and Yussouf and Stensrud [2010]. This weighted, volume-averaged value effectively becomes the reflectivity “observed” by the simulated radar at that particular range bin along the central beam. All beam interpolations and averaging are conducted in linear units of Z_e . Note that the algorithm does not account for any two-way attenuation (i.e., signal power loss) due to the absorption by gases and/or scattering by cloud and precipitation particles that are known to occur along the beam path in both the outgoing and returning signal directions. Additionally, the algorithm does not account for noise, side-lobe effects, or ground clutter.

Acknowledgments

Michael Whimpey (CAWCR) and Scott Collis (formerly CAWCR, now at Argonne National Laboratory) are gratefully acknowledged for providing the gridded C-POL data and radar geometry files, respectively. Harald Richter (CAWCR) is acknowledged for constructive comments on an earlier version of this manuscript. The work was funded in part by the Australian Research Council's Future Fellowships (FT0990892) and Centre of Excellence (CE110001028) schemes. The lead author also acknowledges the support of the Australian Postgraduate Award scheme when this study was undertaken. The Victorian Partnership for Advanced Computing (VPAC) provided high-performance computing facilities. Finally, the authors wish to thank the three anonymous reviewers for their comments that helped improve the paper.

References

- Arnold, C. P., Jr., and C. H. Dey (1986), Observing-Systems Simulation Experiments: Past, present, and future, *Bull. Am. Meteorol. Soc.*, **67**(6), 687–695.
- Atlas, R. M. (1997), Observing System Simulation Experiments: Methodology, examples and limitations, *CGC/WMO Work. Geneva, Switz.*, (WMO TD No. 868).
- Bedka, K., J. Brunner, R. Dworak, W. Feltz, J. Otkin, and T. Greenwald (2010), Objective satellite-based detection of overshooting tops using infrared window channel brightness temperature gradients, *J. Appl. Meteorol. Climatol.*, **49**(2), 181–202, doi:10.1175/2009JAMC2286.1.
- Blahak, U. (2008), An approximation to the effective beam weighting function for scanning meteorological radars with an axisymmetric antenna pattern, *J. Atmos. Oceanic Technol.*, **25**, 1182–1196, doi:10.1175/2007JTECHA1010.1.
- Caine, S., C. Jakob, S. Siems, and P. May (2009), Objective classification of precipitating convective regimes using a weather radar in Darwin, Australia, *Mon. Weather Rev.*, **137**(5), 1585–1600, doi:10.1175/2008MWR2532.1.
- Caine, S., T. P. Lane, P. T. May, C. Jakob, S. T. Siems, M. J. Manton, and J. Pinto (2013), Statistical assessment of tropical convection-permitting model simulations using a cell-tracking algorithm, *Mon. Weather Rev.*, **141**(2), 557–581, doi:10.1175/MWR-D-11-00274.1.
- Chaboureaud, J.-P., J.-P. Cammas, J. Duron, P. J. Mascart, N. M. Sitnikov, and H.-J. Voessing (2007), A numerical study of tropical cross-tropopause transport by convective overshoots, *Atmos. Chem. Phys.*, **7**(7), 1731–1740.
- Chemel, C., M. R. Russo, J. A. Pyle, R. S. Sokhi, and C. Schiller (2009), Quantifying the imprint of a severe Hector thunderstorm during ACTIVE/SCOUT-03 onto the water content in the upper troposphere/lower stratosphere, *Mon. Weather Rev.*, **137**(8), 2493–2514, doi:10.1175/2008MWR2666.1.
- Corti, T., et al. (2008), Unprecedented evidence for deep convection hydrating the tropical stratosphere, *Geophys. Res. Lett.*, **35**, L10810, doi:10.1029/2008GL033641.
- de Reus, M., et al. (2009), Evidence for ice particles in the tropical stratosphere from in-situ measurements, *Atmos. Chem. Phys.*, **9**(18), 6775–6792.
- Dee, D. P., et al. (2011), The ERA-Interim reanalysis: Configuration and performance of the data assimilation system, *Q. J. R. Meteorol. Soc.*, **137**(656), 553–597, doi:10.1002/qj.828.
- Drosowsky, W. (1996), Variability of the Australian summer monsoon at Darwin: 1952–1997, *J. Clim.*, **9**, 85–96.
- Dworak, R., K. Bedka, J. Brunner, and W. Feltz (2012), Comparison between GOES-12 overshooting-top detections, WSR-88D radar reflectivity, and severe storm reports, *Weather Forecasting*, **27**(3), 684–699, doi:10.1175/WAF-D-11-00070.1.
- Frederick, K., and C. Schumacher (2008), Anvil characteristics as seen by C-POL during the Tropical Warm Pool International Cloud Experiment (TWP-ICE), *Mon. Weather Rev.*, **136**(1), 206–222, doi:10.1175/2007MWR2068.1.
- Fueglistaler, S., A. E. Dessler, T. J. Dunkerton, I. Folkins, Q. Fu, and P. W. Mote (2009), Tropical tropopause layer, *Rev. Geophys.*, **47**, RG1004, doi:10.1029/2008RG000267.
- Grosvenor, D. P., T. W. Choulartan, H. Coe, and G. Held (2007), A study of the effect of overshooting deep convection on the water content of the TTL and lower stratosphere from Cloud Resolving Model simulations, *Atmos. Chem. Phys.*, **7**, 4977–5002.
- Hassim, M. E. E. (2012), The influence and observability of overshooting convection in the tropical tropopause layer, PhD thesis, School of Earth Sciences, The University of Melbourne, Available from <http://repository.unimelb.edu.au/10187/15389>.
- Hassim, M. E. E., and T. P. Lane (2010), A model study on the influence of overshooting convection on TTL water vapour, *Atmos. Chem. Phys.*, **10**(20), 9833–9849, doi:10.5194/acp-10-9833-2010.
- Hume, T. (2007), Radiation dry bias in the TWP-ICE radiosonde soundings, in *Proc. 17th ARM Sci. Team Meet.*, Atmospheric Radiation Measurement (ARM) Program, Monterey, Calif. [Available online at <http://www.arm.gov/publications/proceedings/conf17/poster/P00011.pdf>].
- Jensen, E. J., A. S. Ackerman, and J. A. Smith (2007), Can overshooting convection dehydrate the tropical tropopause layer?, *J. Geophys. Res.*, **112**, D11209, doi:10.1029/2006JD007943.
- Keenan, T., K. Glasson, F. Cummings, T. S. Bird, J. Keeler, and J. Lutz (1998), The BMRC/NCAR C-band polarimetric (C-POL) radar system, *J. Atmos. Oceanic Technol.*, **15**, 871–886.
- Keenan, T. D., and R. E. Carbone (1992), A preliminary morphology of precipitation systems in tropical northern Australia, *Q. J. R. Meteorol. Soc.*, **118**(504), 283–326, doi:10.1002/qj.49711850406.
- Kummerow, C., W. Barnes, T. Kozu, J. Shiue, and J. Simpson (1998), The Tropical Rainfall Measuring Mission (TRMM) sensor package, *J. Atmos. Oceanic Technol.*, **15**(3), 809–817, doi:10.1175/1520-0426(1998)015<0809:TTRMMT>2.0.CO;2.

- Liu, C., and E. J. Zipser (2005), Global distribution of convection penetrating the tropical tropopause, *J. Geophys. Res.*, **110**, D23104, doi:10.1029/2005JD006063.
- Liu, C., E. J. Zipser, and S. W. Nesbitt (2007), Global distribution of tropical deep convection: Different perspectives from TRMM infrared and radar data, *J. Clim.*, **20**, 489–503.
- Liu, X. M., E. D. Riviere, V. Maréchal, G. Durry, A. Hamdouni, J. Arteta, and S. Khaykin (2010a), Stratospheric water vapour budget and convection overshooting the tropopause: Modelling study from SCOUT-AMMA, *Atmos. Chem. Phys.*, **10**(17), 8267–8286, doi:10.5194/acp-10-8267-2010.
- Liu, Z., R. Marchand, and T. Ackerman (2010b), A comparison of observations in the tropical western Pacific from ground-based and satellite millimeter-wavelength cloud radars, *J. Geophys. Res.*, **115**, D24206, doi:10.1029/2009JD013575.
- May, P. T., and A. Ballinger (2007), The statistical characteristics of convective cells in a monsoon regime (Darwin, northern Australia), *Mon. Weather Rev.*, **135**(1), 82–92, doi:10.1175/MWR3273.1.
- May, P. T., and T. D. Keenan (2005), Evaluation of microphysical retrievals from polarimetric radar with wind profiler data, *J. Appl. Meteorol.*, **44**, 827–838, doi:10.1175/JAM2230.1.
- May, P. T., and T. P. Lane (2009), A method for using weather radar data to test cloud resolving models, *Meteorol. Appl.*, **16**(3), 425–432, doi:10.1002/met.150.
- May, P. T., and D. K. Rajopadhyaya (1999), Vertical velocity characteristics of deep convection over Darwin, Australia, *Mon. Weather Rev.*, **127**, 1056–1071.
- May, P. T., J. H. Mather, G. Vaughan, K. N. Bower, C. Jakob, G. M. McFarquhar, and G. G. Mace (2008), The Tropical Warm Pool International Cloud Experiment, *Bull. Am. Meteorol. Soc.*, **89**(5), 629–645, doi:10.1175/BAMS-89-5-629.
- May, P. T., C. N. Long, and A. Protat (2012), The diurnal cycle of the boundary layer, convection, clouds, and surface radiation in a coastal monsoon environment (Darwin, Australia), *J. Clim.*, **25**(15), 5309–5326, doi:10.1175/JCLI-D-11-00538.1.
- Mohr, C. G., and R. L. Vaughan (1979), An economical procedure for Cartesian interpolation and display of reflectivity data in three-dimensional space, *J. Appl. Meteorol.*, **18**, 661–670.
- Murphy, D. M., and T. Koop (2005), Review of the vapour pressures of ice and supercooled water for atmospheric applications, *Q. J. R. Meteorol. Soc.*, **131**, 1539–1565.
- Nielsen, J. K., N. Larsen, F. Cairo, G. Di Donfrancesco, J. M. Rosen, G. Durry, G. Held, and J. P. Pommereau (2007), Solid particles in the tropical lowest stratosphere, *Atmos. Chem. Phys.*, **7**(3), 685–695.
- Protat, A., J. Delanoë, A. Plana-Fattori, P. T. May, and E. J. O'Connor (2010), The statistical properties of tropical ice clouds generated by the West African and Australian monsoons, from ground-based radar-lidar observations, *Q. J. R. Meteorol. Soc.*, **136**(S1), 345–363, doi:10.1002/qj.490.
- Roberts, N. M., and H. W. Lean (2008), Scale-selective verification of rainfall accumulations from high-resolution forecasts of convective events, *Mon. Weather Rev.*, **136**(1), 78–97, doi:10.1175/2007MWR2123.1.
- Seed, A. W., and G. G. S. Pegram (2001), Using Kriging to infill gaps in radar data due to ground clutter in real time, Preprints, *Fifth International Symposium on Hydrological Applications of Weather Radar*, Kyoto, Japan.
- Simpson, J., T. D. Keenan, B. Ferrier, R. H. Simpson, and G. J. Holland (1993), Cumulus mergers in the maritime continent region, *Meteorol. Atmos. Phys.*, **51**, 73–99.
- Skamarock, W. C., J. B. Klemp, J. Dudhia, D. O. Gill, D. M. Baker, M. G. Duda, X.-Y. Huang, W. Wang, and J. G. Powers (2008), A description of the Advanced Research WRF version 3, *NCAR/TN-47*, 113 pp.
- Stephens, G. L., et al. (2008), CloudSat mission: Performance and early science after the first year of operation, *J. Geophys. Res.*, **113**, D00A18, doi:10.1029/2008JD009982.
- Thompson, G., P. R. Field, R. M. Rasmussen, and W. D. Hall (2008), Explicit forecasts of winter precipitation using an improved bulk microphysics scheme. Part II: Implementation of a new snow parameterization, *Mon. Weather Rev.*, **136**(12), 5095–5115, doi:10.1175/2008MWR2387.1.
- Toon, O. B., et al. (2010), Planning, implementation, and first results of the Tropical Composition, Cloud and Climate Coupling Experiment (TC4), *J. Geophys. Res.*, **115**, D00J04, doi:10.1029/2009JD013073.
- Vallgren, A. (2006), Statistical characteristics of convective storms in Darwin, Northern Australia, Master's thesis, Department of Applied Physics and Mechanical Engineering, Luleå University of Technology.
- Varble, A., A. M. Fridlind, E. J. Zipser, A. S. Ackerman, J.-P. Chaboureaud, J. Fan, A. Hill, S. A. McFarlane, J.-P. Pinty, and B. Shipway (2011), Evaluation of cloud-resolving model intercomparison simulations using TWP-ICE observations: Precipitation and cloud structure, *J. Geophys. Res.*, **116**, D12206, doi:10.1029/2010JD015180.
- Vaughan, G., C. Schiller, A. R. MacKenzie, K. Bower, T. Peter, H. Schlager, N. R. P. Harris, and P. T. May (2008), SCOUT-O3/ACTIVE: High-altitude aircraft measurements around deep tropical convection, *Bull. Am. Meteorol. Soc.*, **89**(5), 647–662.
- Wang, Y., C. N. Long, L. R. Leung, J. Dudhia, S. A. McFarlane, J. H. Mather, S. J. Ghan, and X. Liu (2009), Evaluating regional cloud-permitting simulations of the WRF model for the Tropical Warm Pool International Cloud Experiment (TWP-ICE), Darwin, 2006, *J. Geophys. Res.*, **114**, D21203, doi:10.1029/2009JD012729.
- Wapler, K., T. P. Lane, P. T. May, C. Jakob, M. J. Manton, and S. T. Siems (2010), Cloud-system-resolving model simulations of tropical cloud systems observed during the Tropical Warm Pool-International Cloud Experiment, *Mon. Weather Rev.*, **138**(1), 55–73, doi:10.1175/2009MWR2993.1.
- Wood, V. T., R. A. Brown, and D. Dowell (2009), Simulated WSR-88D velocity and reflectivity signatures of numerically modeled tornadoes, *J. Atmos. Oceanic Technol.*, **26**, 876–893.
- Wu, J., A. D. Del Genio, M.-S. Yao, and A. B. Wolf (2009), WRF and GISS SCM simulations of convective updraft properties during TWP-ICE, *J. Geophys. Res.*, **114**, D04206, doi:10.1029/2008JD010851.
- Yussouf, N., and D. J. Stensrud (2010), Impact of phased-array radar observations over a short assimilation period: Observing system simulation experiments, *Mon. Weather Rev.*, **138**, 517–538, doi:10.1175/2009MWR2925.1.
- Yuter, S. E., and R. A. Houze (1995), Three-dimensional kinematic and microphysical evolution of Florida cumulonimbus. Part II: Frequency distributions of vertical velocity, reflectivity, and differential reflectivity, *Mon. Weather Rev.*, **123**(7), 1941–1963, doi:10.1175/1520-0493(1995)123<1941:TDKAME>2.0.CO;2.